Continuum model for the growth of interfaces

Pawel Keblinski,[1,*] Amos Maritan,[2] Flavio Toigo,[3] Russell Messier,[4] and Jayanth R. Banavar[1]
[1]*Department of Physics and Center for Material Physics, 104 Davey Laboratory, The Pennsylvania State University, University Park, Pennsylvania 16802;*
[2]*International School for Advanced Studies, via Beirut 4, 34014 Trieste, Italy; Istituto Nazionale di Fisica Nucleare, Sezione di Trieste, Trieste, Italy; and Istituto Nazionale per la Fisica della Materia, Unita di Trieste, Trieste, Italy;*
[3]*Dipartimento di Fisica and Istituto Nazionale per la Fisica della Materia INFM, via Marzolo 8, 35100 Padova, Italy;*
[4]*Department of Engineering Science and Mechanics, 265 Materials Research Laboratory, The Pennsylvania State University, University Park, Pennsylvania 16802*
(Received 30 May 1995)

A continuum model is presented for studying various growth processes. One of the model equations is used to define a growing interface with an arbitrary topology and captures the intrinsic dynamics of the aggregate with surface diffusion incorporated in a natural manner. With an appropriate local growth mechanism, this model represents a continuum version of the Eden growth model. The introduction of another field describing the dynamics of the vapor enables the modeling of phenomena ranging from ballistic deposition to diffusion-limited aggregation (DLA) within the framework of the same equations. Our equations capture nonlocal effects, such as shadowing or screening in a local way, and permit the monitoring of the interior structure of the growing film. Our results are benchmarked against those of experiments on sputter deposited films. Simple modifications of the model lead to patterns that are different from standard DLA structures but similar to those observed in electrochemical deposition. We also examine models that use the no-overhang approximation in the description of columnar morphology observed in thin films and discuss their validity in comparison with our model.

PACS number(s): 81.10.Aj, 05.40.+j, 64.60.Ht, 05.70.Ln

I. INTRODUCTION

The dynamics and morphology of growing clusters and films have been the focus of intense research in the last decade [1]. Interest in this field is driven primarily by two factors. First, growth processes, especially involving molecular beam epitaxy (MBE) or sputter deposition, are technologically important. Second, these growth processes are a prototype of fundamental problems in nonequilibrium statistical physics that often do not have a Hamiltonian formulation.

A wide variety of processes, both natural and technological, lead to intricate structures having complex morphologies. However, many of them show striking similarities suggesting an underlying universality. Examples include biological growth, corrosion, electrodeposition, fluid flow through porous media, vapor deposition, aggregation processes, crystal growth, the propagation of flame fronts, and directed polymers in a random medium.

A fundamental question is whether these seemingly diverse systems have an underlying universality—are they described by the same physics? In recent years, some progress has been made toward answering this question by means of experiment, analytic theories, and computer simulations. Scaling regions and universality classes have been identified for the simplest class of problems—those that do not involve nonlocal effects [2] such as screening or shadowing. However, it is interesting to note that disagreements remain between theory and experiment [1].

One example of universal behavior is observed in thin films prepared under low adatom mobility. They have common morphologies, relatively independent of material composition [3–9]. Changes in the morphology of thin films are directly linked to corresponding wide variations in their resulting physical properties, and have important ramifications in applications such as coated cutting tools, optical coatings, and optical and magnetic storage media. Another example of such universality is observed in processes such as viscous flow and electrochemical deposition [10-18]. In those cases, growing clusters can be described within the framework of diffusion-limited aggregation (DLA) [10]. In vapor-deposited films or DLA-type phenomena, nonlocal effects play a crucial role in determining the dynamics of growth and the resulting morphology.

The modeling of the growth of stochastic interfaces can be classified into two major categories.

(i) Discrete "toy" models where particles move and are deposited according to physically motivated rules—examples include a number of solid models [1], ballistic deposition [19], and the original DLA model [10]. The discrete description does not incorporate surface diffusion in a natural way.

(ii) A continuum description of the growth by use of

*Present address: Argonne National Laboratory, MSD/212, Argonne, IL 60439.

partial differential equations (PDE's) [1]. Usually the position of the interface is represented as a single-valued function of the substrate coordinates (no-overhang approximation). This approach is accessible to analytical treatment usually by dynamical renormalization group (RG) methods, but is limited to the no-overhang approximation and does not accommodate nonlocal effects.

More realistic molecular dynamics simulations [20] are limited to small sizes of the system. A majority of the approaches to growth modeling disregards the morphology of the aggregate interior and focuses exclusively on the interfacial structure.

In this paper we present the results of a detailed study of a model that was introduced in our recent publications [21–23] and which is able to provide a unified picture of several growth processes. In addition, we analyze other models that describe the morphology of the growing films within a no-overhang approximation, and discuss their validity by comparing these results with our findings. We build our model on the basis of simple physical requirements. Our model is a continuum approach that allows for an arbitrary topology of the interface, contrary to the computationally convenient but not always justified no-overhang approximation. Further, surface tension is incorporated into our model in a natural manner. The model enables the study of different dynamics of the vapor depositing on the aggregate. Nonlocal effects like shadowing or screening are included in a local way. We can also monitor the structure of the interior of the aggregate. Our model is able to describe phenomena such as Eden growth, ballistic deposition, and DLA within the framework of the same equations.

In Sec. II we introduce a model with a phase field whose dynamics corresponds to that of a conserved order parameter. Two equilibrium values of the field describe the aggregate and the vapor regions. This allows one to define the interface with an arbitrary topology and builds the correct physics for surface tension (it takes into account both surface and bulk diffusion). With a local growth term characterized by a constant rate of aggregation per unit length of the interface, our model is in the Kardar-Parisi-Zhang universality class [24]. However, if the local growth rate depends on the interfacial curvature we observe different dynamics of the growth. In Sec. III, in addition to the field describing the dynamics of the interface, we introduce another field to incorporate the dynamics of the vapor and nonlocal effects. The coupling between the two fields provides for the growth of the aggregate at the expense of the vapor. In this section we study the growth with ballistic trajectories of the incoming atoms. We observe changes in the morphology on varying the strength and angle of the incoming rain. Our results are benchmarked against those of experiments on sputter-deposited films. Section IV discusses models that attempt to explain the columnar morphology observed in thin films within the no-overhang approximation. We extend the model proposed by Golubovic and Karunasiri [25] to situations in which the incidence of the incoming vapor is oblique. Finally, Sec. V considers the description of DLA-type phenomena within the framework of our model. In particular, a comparison with the patterns produced in experiments on electrochemical deposition [18] is presented.

II. CONTINUUM GROWTH MODELS WITH AN ARBITRARY TOPOLOGY OF THE INTERFACE

A simple continuum model that is believed to capture the physics of processes such as ballistic deposition [19] (in the basic version, particles follow linear trajectories and stick to the aggregate upon the first encounter), or the Eden model (each point adjacent to the aggregate interface is equally likely to grow) is the Kardar-Parisi-Zhang (KPZ) [24] equation

$$\frac{\partial h}{\partial t}=\nu\nabla^2 h+\frac{\lambda}{2}(\nabla h)^2+\eta(\mathbf{r},t)\ , \tag{1}$$

where the height $h(\mathbf{x},t)$ is a single-valued function of the spatial coordinate $\mathbf{x}$, and ν is a height diffusion term that could describe the influence of a gravitational field acting on the aggregate or the effects of the evaporation-condensation process. The λ term describes the growth normal to the interface [the lowest order nontrivial term in a $(\nabla h)^2$ expansion], and η is a Gaussian noise with zero mean and $\langle \eta(\mathbf{x},t)\eta(\mathbf{x}',t')\rangle = 2D\delta^d(\mathbf{x}-\mathbf{x}')\delta(t-t')$. Surface diffusion can be incorporated into Eq. (1) by adding a $-k\nabla^4 h$ term to the right hand side of the equation. The surface diffusion term is responsible for local smoothing of the interface—however, in the large length scale limit its effects are irrelevant as long as the other two terms are not identically zero.

In this section we present a simple local continuum model that allows for overhangs and arbitrary topology of the growing interfaces. The model captures surface diffusion in a natural manner and, with an appropriate aggregation mechanism, it produces growth normal to the interface. The model equation consists of two parts; the first is a conserved order parameter dynamics that allows for the definition of a topologically unrestricted interface and builds the correct physics of surface diffusion, whereas the second term provides the growth and roughening at the interface.

Our equations are

$$\frac{\partial f(\mathbf{r},t)}{\partial t}=\Gamma\nabla^2\frac{\delta F}{\delta f(\mathbf{r},t)}+I\ , \tag{2}$$

where

$$F=\int\left[-\frac{1}{2}f^2+\frac{f^4}{4}+a(\nabla f)^2\right]dv\ . \tag{3}$$

Equation (2) without the I term has a simple interpretation—it is merely the deterministic part of the standard model B dynamics [26] that conserves the order parameter.

The choice of the sign of the coefficient of f^2 in the expansion for the free energy (3) corresponds to a temperature lower than T_c, so that the two values of the order parameter $f(\mathbf{r},t)$ minimizing the free energy describe the two equilibrium phases of the system. The equilibrium values of the order parameter have been set to ± 1 by an

appropriate choice of its units of measurement.

In $d=1+1$, the vector $\mathbf{r}$ has two components x and z, whereas in $d=2+1$, $\mathbf{r}=(x,y,z)$. In our numerical study of Eq. (3) we use as the initial configuration for f the equilibrium profile that satisfies the equation $\delta F/\delta f=0$ with boundary conditions $\lim_{z\to\pm\infty} f=\pm 1$. These boundary conditions are maintained during the growth.

An interface can naturally be defined as the crossover region between the $f=-1$ and $f=+1$ regions— and, operationally, a point $\mathbf{r}_i$ is defined to be on the surface when $f(\mathbf{r}_i,t)=0$. $a>0$ is the surface diffusion coefficient and sets the intrinsic length in the system. Indeed, the width of the interface is proportional to $\sqrt{a}$. Also, the effective strength of the surface tension turns out to be proportional to $\sqrt{a}$. By an appropriate choice of time scale, the mobility coefficient Γ may be set [27] equal to 1.

The I term allows for the growth and fluctuations of the interface. We utilize two different forms of the I term:

$$I_1=C_1|\nabla f|+D_1\sqrt{|\nabla f|}\eta(r,t) \tag{4}$$

and

$$I_2=|\nabla f|^2[C_2+D_2\eta(r,t)]\ , \tag{5}$$

where η is a Gaussian noise uncorrelated in time and space with a width equal to 1, and a mean value 0. In both growth terms, the ∇f factor ensures that the growth and fluctuations are operative only in the vicinity of the interface—away from the interface ∇f is equal to zero. The positive coefficients C and D are the magnitudes of the growth and noise, respectively. The growth term is restricted to the region $|f|<b$, where b is close to but less than 1. In the region filled by the aggregate the f value fluctuates around $f=+1$ so that, without this restriction, the positive contribution from the growth term causes an unbounded increase of f above the equilibrium value especially for the long runs. In the majority of our runs we used $b=0.9$. The ∇f factor also produces growth normal to the interface, which is illustrated in Fig. 1. The evolution of an initial rectangular bump shows that the growth is normal to the interface with the initially sharp corners being smoothed by the surface diffusion.

The numerical results show that our model with the I_1 growth mechanism is in the same universality class as the KPZ equation, whereas the model with an I_2 growth term exhibits different dynamical scaling behavior. The I_1 growth mechanism not only gives growth normal to the interface, but also the rate of the growth per unit length is constant along the interface, equal to $C_1\int_{s_{\min}}^{s_{\max}}|\nabla f|ds=2bC_1$, where the integral is performed across the interface and $s_{\min}$ and $s_{\max}$ are defined by $f(s_{\min})=-b$ and $f(s_{\max})=b$ (note that the integral is independent of the shape of the ∇f profile as long as f increases monotonically from $f=-1$ to $f=+1$). This feature leads to KPZ-like behavior.

We use a model with local conservation to avoid the formation of islands with $f=-1$ in the region predominantly with $f=+1$, and vice versa. The conserved and nonconserved models should exhibit interfaces with the same behavior. In the Appendix, we will show that the nonconserved version of the I_1 model is equivalent to the KPZ equation when the interface is sharp, i.e., a is small.

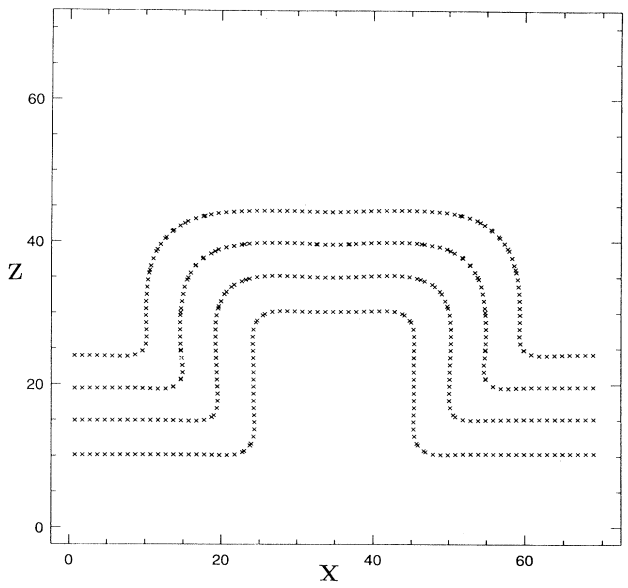

FIG. 1. Sequence of interfaces generated from Eq. (2) with the I_1 growth mechanism noise term turned off, and $a=\frac{1}{2}$ in $d=1+1$ showing the evolution of rectangular bump.

Thus we may interpret the I_1 growth as a continuum version of the Eden growth model, with a redistribution of the aggregated particles via surface diffusion.

The Eden model is known to be in the KPZ universality class—the surface diffusion in the limit of large length scales does not change the geometrical properties of the interface, but introduces a short range smoothing mechanism.

The I_2 growth mechanism does not have the property of a uniform growth rate. The effective growth, as our results show, depends on the local curvature of the interface, and leads to an increase of the growth exponent β with time.

We studied our model in $d=1+1$ and $d=2+1$ dimensions. We have solved Eq. (2) on a square lattice (cubic in $d=2+1$) with a lattice constant equal to 1. In our numerical solution we used Euler's method with an integration time step of 0.01 in order to avoid numerical instabilities [27]. Statistically similar results were found for several runs in which the time step was reduced by a factor of 2. The Laplacian term in our simulations was calculated as

$$\Delta f=\left[\sum_{NN} f(\mathbf{r}_{\mathrm{NN}},t)\right]-qf(\mathbf{r},t)\ ,$$

where the sum is performed over the nearest neighbors, and q is the coordination number equal to 4 in $d=1+1$

and 6 in $d=2+1$, respectively. An interpolation scheme to locate the interface leads to a resolution an order of magnitude finer than the lattice constant. We use periodic boundary conditions in a direction transverse to the initially flat interface located in the middle of the sample. The edges of the system in the growth direction z, having the values $f=\pm 1$ were matched with antiperiodic boundary conditions. Typical values of C (the growth term) and D (the noise term) were of order 1. Smaller values of these parameters lead to the roughness being smaller than $\sqrt{a}$, the natural width of the equilibrated interface, whereas values of the parameters several times larger lead to instabilities in the numerical solution of Eq. (2).

Figure 2 shows typical profiles of the evolving interface with the I_2 growth mechanism. The interface has overhangs—they occasionally merge, leaving holes behind. The holes are filled up due to the growth mechanism and do not play any role in the further evolution of the interface. Similar interfacial profiles are obtained with the I_1 growth term. Figure 3 shows a power law growth of the width of the interface—W in $d=1+1$ and $d=2+1$ for the I_1 growth mechanism ($W \propto t^{\beta}$ at early stages of the aggregation). A least squares linear fit of the log-log plot gives the growth exponent $\beta=0.34\pm0.01$ in $d=1+1$ and $\beta=0.24\pm0.02$ in $d=2+1$. At saturation, the width of the interface scales with the lateral size of the substrate $W \propto L^{\alpha}$. The estimate for the exponent α in $d=1+1$ is 0.51 ± 0.03. These results are in agreement with the exact solution of the KPZ equation [24] in $d=1+1$, $\beta=\frac{1}{3}$, and $\alpha=\frac{1}{2}$. The β exponent in $d=2+1$ is consistent with the numerical solution of the KPZ equation and the Kim-Kosterlitz estimates [28]. The data are averages over 100 systems in $d=1+1$, and ten systems in

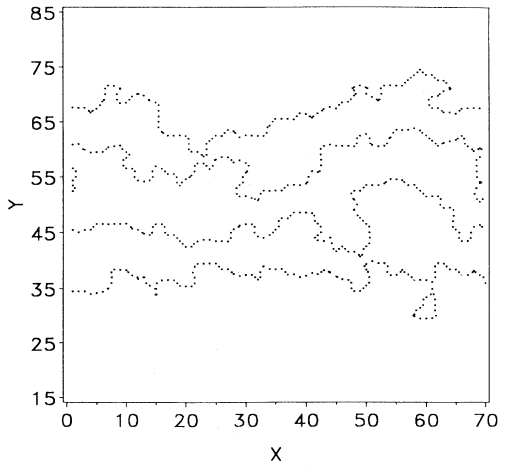

FIG. 2. Sequence of the interfaces generated from Eq. (2) every 15 time units with the I_2 growth mechanism and $a=\frac{1}{4}$ and $d=1+1$. The location of the interface was determined by solving for $f\equiv 0$. The third contour from the bottom has a hole at the boundary, where periodic boundary conditions are applied.

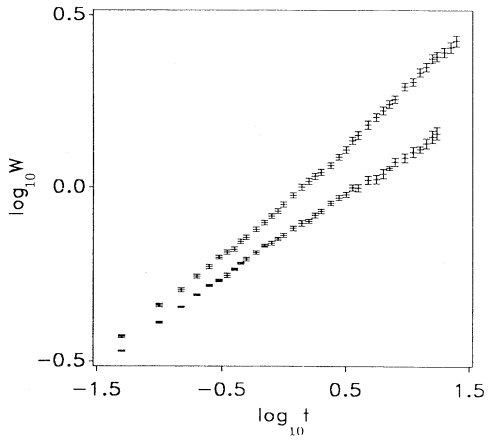

FIG. 3. Interface width as a function of time for $a=1$, I_1 growth mechanism. Upper data correspond to $d=1+1$, and lower to $d=2+1$. Data are for lateral size 100 in $d=1+1$ and 40×40 in $d=2+1$. Data are averaged over 100 and ten runs, respectively.

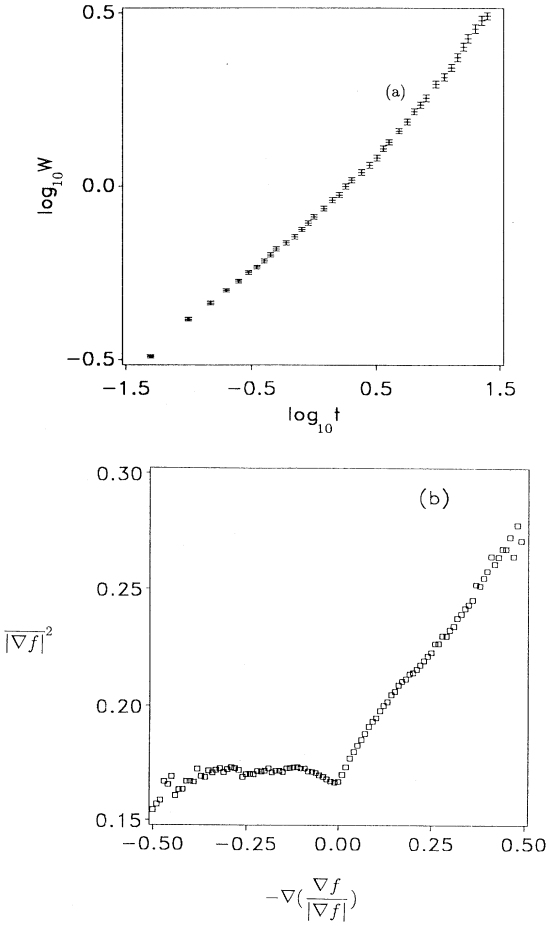

FIG. 4. (a) Log-log plot of width vs time for the I_2 growth mechanism with $a=1$ in $d=1+1$; the lateral size is 100. (b) Average value of $(\nabla f)^2$ vs curvature of the interface $(-\nabla\cdot\nabla f/|\nabla f|)$; data are averages for 30 samples, and all other parameters are the same as in (a).

$d=2+1$. Due to computational limitations we were unable to estimate α in $d=2+1$.

Figure 4(a) shows the growth of the roughness vs time on a log-log scale for the I_2 growth mechanism (data are averages over 100 samples). The saturation width of the interface scales as $L^{0.53\pm0.03}$, which is, within the statistical error, the same exponent as in the I_1 growth mechanism. However, the dynamical behavior is different. The β exponent increases from 0.3 initially to 0.5 at the largest time we access in our simulations. In order to understand the origin of this phenomena, we study the correlation between ∇f and the curvature of the interface,

$$-\nabla\cdot\left[\frac{\nabla f}{|\nabla f|}\right] \tag{6}$$

(note that the ∇f vector is directed toward the $f=1$ region). Figure 4(b) shows a plot of the average value of ∇f vs curvature. In the negative curvature region, ∇f is fairly constant, while in the positive region it increases sharply with curvature. The higher value of ∇f corresponds to a steeper crossover from the $f=-1$ to the $f=+1$ region, and it translates into a larger growth rate per unit length in the positive curvature region. Figure 4(b) suggests that the more advanced parts of the interface have steeper crossover between the two phases of the f field, while the zero and negative curvature regions have this crossover smoothed out since they have more time to be relaxed by the surface tension. Initially, when the curvature is low, β is close to the $\frac{1}{3}$ value. Later the effects of the large curvature speed up the roughening of the interface. If the growth mechanism is proportional to an even higher power of ∇f, one may expect behavior analogous to "dielectric breakdown" with high curvature regions growing much more rapidly than the rest of the interface.

In this section we have introduced a simple model described by Eqs. (2) and (3) that provides a simple framework for a description of the dynamics of interfaces having arbitrary topologies. The simple analog of the KPZ-type dynamics shows that the presence of overhangs does not produce a new universality class. Nevertheless as shown in Sec. III, overhangs do play a crucial role in a detailed description of the morphology of the aggregate, and they influence the structure of the interface when nonlocal effects are important. We have shown in this section that even within a local growth model, if the growth rate is a function of the curvature, the dynamics of the interfacial evolution is altered from KPZ-type behavior.

III. BALLISTIC DEPOSITION

In Sec. II, we introduced a model with a local growth mechanism that allows for an arbitrary topology of the interface. The growth of real surfaces is often influenced by nonlocal effects like screening or shadowing. When the aggregating particles follow linear trajectories one can expect that, if the roughness is large enough, some parts of the interface are shadowed and, therefore, do not grow. In order to accommodate this phenomenon we now extend our model to incorporate the dynamics of the depositing vapor and nonlocal effects. We study the three geometries of the incident vapor that are depicted in Fig. 5.

Our extended model involves two fields f and g, and is governed by the equations

$$\frac{\partial f(\mathbf{r},t)}{\partial t}=\nabla^2\frac{\delta F}{\delta f(\mathbf{r},t)}+B(\nabla f)^2 g(\mathbf{r},t) + C\sqrt{(\nabla f)^2 g}\,\eta(\mathbf{r},t)\ , \tag{7}$$

$$\frac{\partial g(r,t)}{\partial t}=\nabla[D\nabla g(\mathbf{r},t)-\mathbf{A}g(\mathbf{r},t)]-B(\nabla f)^2 g(\mathbf{r},t)\ , \tag{8}$$

with F again given by Eq. (3). While the first part of Eq. (7) is identical to that in Sec. II, the growth mechanism is different. Now the growth of the f field occurs at the expense of the g field. The g field represents the local density of the incoming particles toward the interface, and Eq. (8) describes the dynamics of the depositing vapor. The first part of Eq. (8) is simply the diffusion equation in the presence of an external force $\mathbf{A}$. In order to analyze the growth arising from ballistic trajectories D was chosen much smaller than $\mathbf{A}$ so the $\mathbf{A}g$ flux is the primary mechanism for g field transport. Setting $D=0$ causes singularities and destabilizes the numerical solution of Eqs. (7) and (8). The aggregation relies on the conversion of the g field into the f field as described by the coupling term B in (7) and (8). The ∇f factor in the B term makes the aggregation operative only within an interfacial "skin" region of the aggregate with its width proportional to $\sqrt{a}$. The g factor in the aggregation term ensures that the growth occurs only if $g>0$. The B term acts as a sink for the diffusive field g, and its magnitude is chosen to be sufficiently large to convert all of the g into f within the interfacial region effectively leading to $g\sim0$ below the interface ($f\sim+1$). Shadowing effects are naturally incorporated in our equations. When the g field trajectory intercepts the skin, the g field is converted into f, and any subsequent interception occurs with $g=0$ and, therefore, does not lead to the growth of the shadowed part of the interface. Note that nonlocal effects are incorporated in a local way in Eqs. (7) and (8). One does not need to monitor the geometry of the interface to incorporate shadowing—it is implemented dynamically by the g field. The conversion of the g field into the f field at the vicinity of the interface does not depend crucially on the particular functional form of the coupling chosen. The rate

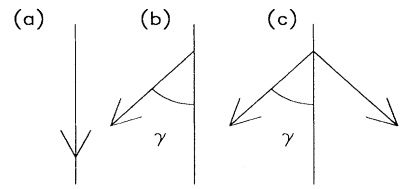

FIG. 5. Schematic depiction of the three geometries of rain: (a) vertical rain, (b) off-vertical rain, and (c) two-rain deposition.

of growth is effectively equal to the intensity of the incoming g field flux. In addition to the growth term, we introduce a fluctuation term C in Eq. (7) with its amplitude proportional to the square root of the aggregation rate, following the central limit theorem. The Gaussian $\eta(\mathbf{r},t)$ factor is the same as was introduced in Sec. II. In this manner, we incorporate the fluctuations into the strength of the incoming g flux, since the aggregation rate is equal to the intensity of the incoming g flux.

The initial configuration for the f field is the same as in Sec. II. The g field is equal to g_0 in the $f<0$ region and $g=0$ when $f>0$. During the simulations, the $g=g_0$ condition is maintained at the upper boundary providing a constant downward flux $\mathbf{A}_g$ during the aggregation process. In order to take into account the lower capture probability of the g field in the regions with f close to -1 (predominantly vapor regions), we allow for the conversion only if $f>b$. In the majority of our simulations we chose $b=-0.2$. In some runs we relaxed this restriction to enhance the mechanism that leads to the columnar instabilities that we discuss below. The method and details of the numerical solution are the same as in Sec. II. A majority of the calculations was performed in $d=1+1$, and some results in $d=2+1$ are also presented.

In order to investigate the simplest case of vertical rain deposition, we took $\mathbf{A}=-A\hat{z}$. The flux is directed vertically downwards, and represents a continuum analog of the incident particles in ballistic deposition growth. In addition to simple ballistic deposition, the g particles are redistributed after deposition via a surface diffusion process. We monitor the growth of the interfacial roughness (the interface is defined as $f=0$) in $d=1+1$ and $d=2+1$. The interfaces are found to be self-affine with the roughness exponent $\alpha=0.51\pm0.03$, and the growth exponent $\beta=0.32\pm0.01$ in $d=1+1$ (Fig. 6). This is in agreement with the results of the KPZ equation [24]. In $d=2+1$ we found $\beta=0.20\pm0.02$ (Fig. 6), which is lower than the 0.240 ± 0.005 value obtained by numerical solution of the KPZ equation [28] and found in the previous section. A result similar to ours was found in off lattice ballistic deposition simulations [29]. It suggests that ballistic deposition may not be in the KPZ universality class for dimensions higher than $1+1$. However, crossover effects could also be responsible for this somehow lower value of β in $d=2+1$. Due to computational limitations we were unable to estimate α in $d=2+1$.

Even when the interface, defined by $f=0$, does not exhibit overhanging configurations when the rain is vertical, the density profiles of the interior of the growing film show a complex morphology. We can naturally define the local density of the aggregate $d_A=(f+1)/2$. With this definition the $f=+1$ region corresponds to the maximum density equal to 1, while $f=-1$ represents a zero density region where the vapor exists. Figure 7 shows density profiles in the film interior for vertically deposited rain. The interior of the sample has a rich structure with visible overhanging configurations. High density regions shadow lower density regions even in the case of vertical deposition. The richness of the morphology originates from destabilizing effects of the nonzero skin width. The skin represents an active region within which capture of the depositing particles take place even when the local normal makes a large angle with the flux directions. This factor causes faster growth of parts of the interface with negative curvature leading to instabilities and shadowing. Similar effects were studied by Mazor *et al.*, [30], where the faster growth of the hills than of the valleys originated from the finite size of the particles. To study the phys-

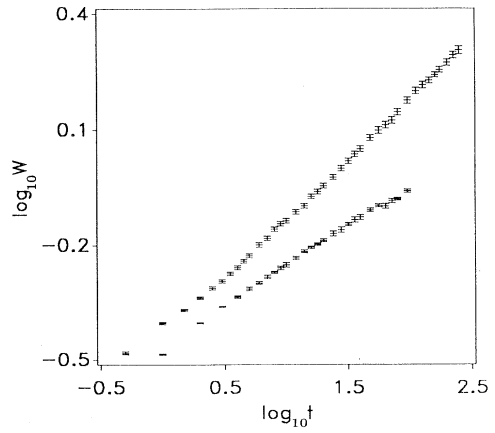

FIG. 6. Interfacial width as a function of time for vertical deposition for $a=\frac{1}{2}$ and $g_0A_z=0.5$. Lower data correspond to $d=2+1$, lateral size 40×40, averaged over 25 samples. In $d=1+1$ (upper curve), the results are for lateral size 150 (averaged over 100 samples).

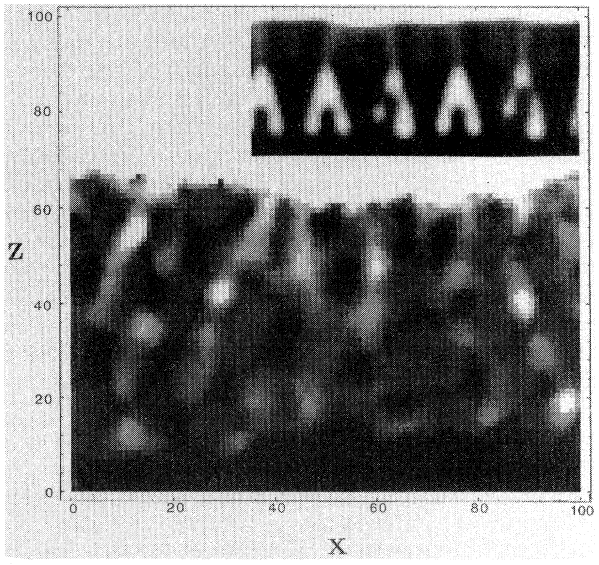

FIG. 7. Density profiles for vertical rain deposition growth (darkest regions correspond to $f=1$). The surface tension coefficient $a=\frac{1}{2}$; $A_zg_0=4.0$. The inset shows the growth of an initially structured substrate without the noise term present.

ics of this phenomenon, Mazor *et al.* proposed a simple equation that captures instabilities due to the finite size of the particles. The solution of their equation leads to a columnar structure of the interface, with the sidewalls of the columns being almost vertical. Similar effects were also studied by Golubovic and Karunasiri [25] (see Sec. IV). In both the above approaches the position of the interface $h=h(x,t)$ is a single-valued function of the lateral substrate coordinate x. Therefore columns cannot merge at the top. Our model has no such restriction—the instability creates columns but they can and do merge as seen clearly in Fig. 7. Our skin plays a dual role. It provides the instabilities studied by Mazor *et al.* but also has a stabilizing merging mechanism. This effect is visually presented in the inset of Fig. 7, where we allow for the conversion being operative deep into the $f<0$ region, thus enhancing the destabilizing skin effect. Now columns flare outwards and finally merge with each other. This inset also shows the importance of shadowing even in this vertical rain situation.

We have reobtained the KPZ results in the limit of low rain intensity and relatively weak destabilizing skin effect. On increasing the rain intensity and the effect of the skin, we observe the development of the columnar structures of the type shown in the inset of Fig. 7, even when we start from a flat interface. Figure 8 shows a log-log plot of the interfacial width vs time for a flux rate $A_z g_0=1$ in $d=1+1$ and with the conversion mechanism operative in the $f\geq 0.8$ region. Initially the growth of the width of the interface follows the KPZ growth exponent. But later, due to the development of the columns, the β exponent crosses over to a value of 1. The roughness exponent ~ 1 has been observed experimentally in a variety of semiconductor materials grown by MBE at low temperatures [31] and in the evolution of ion-beam sputtering erosion of graphite [32]. Our findings show clearly why the KPZ equation is not able to access this aspect of experimental growth—it simply does not allow for overhangs. On the other hand, discrete ballistic deposition does not incorporate surface diffusion in a natural manner, and also misses the feature of growth.

Figure 9 shows growth similar to the one in the inset of Fig. 7 but with 10 times lower rain intensity (upper panel). Now columns grow vertically upward rather than outward. With a very low rain intensity (lower panel of Fig. 9) surface diffusion is able to eliminate the columnar structure altogether. The interface is essentially flat, and the interior of the film has no structure. Such transitions have been observed experimentally in sputter-deposited films. Figure 10 shows a scanning electron micrograph of the top interface of a sputtered amorphous germanium (*a*-Ge) film grown on smooth glass substrates in a diffusion-pumped rf sputtering system with a base pressure of 2×10^{-7} Torr using argon purified with a titanium getter. The sputtering power was 50 W in all cases. The sputtering pressure in Ar decreases from the top to the bottom photograph. The decrease of this pressure corre-

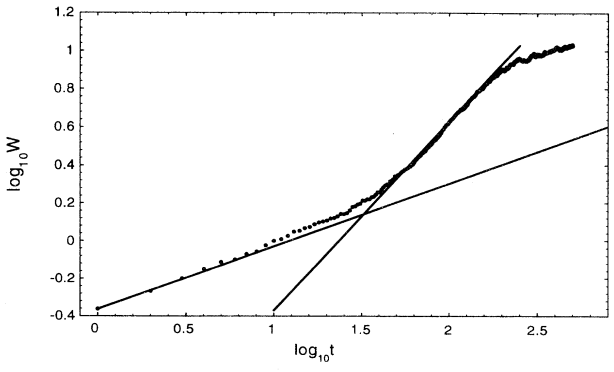

FIG. 8. Log-log plot of the interfacial width as a function of time for vertical deposition with enhanced destabilizing skin effect in $d=1+1$. $a=\frac{1}{2}$ and $A_z g_0=1$. Data are averages over 25 samples of lateral size 100. The solid lines are a guide to the eye and have slopes $\frac{1}{3}$ and 1, respectively.

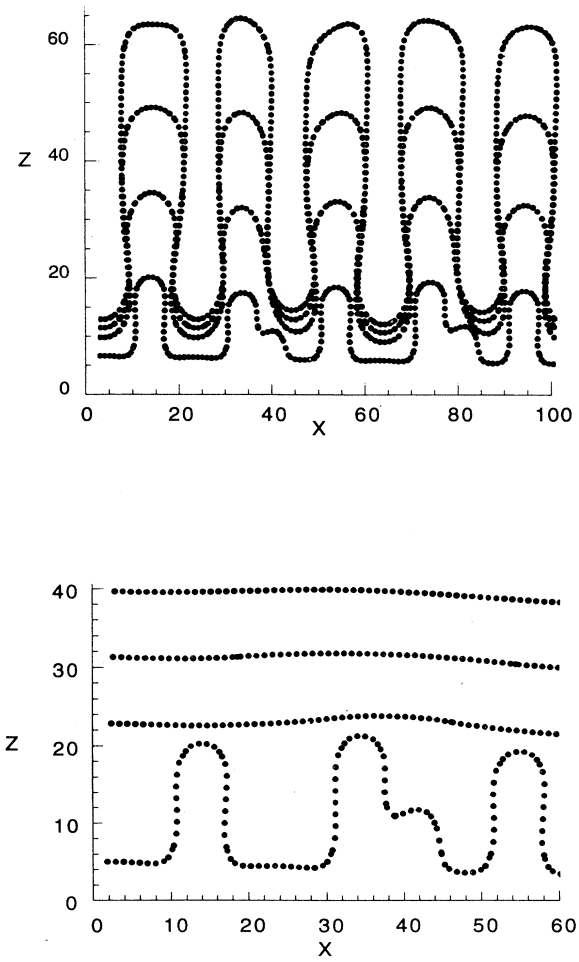

FIG. 9. Interfaces defined as $f=0$ for systems similar to the one shown in the inset of Fig. 7 except for $A_z g_0=0.4$ (upper panel) and $A_z g_0=0.02$ (lower panel).

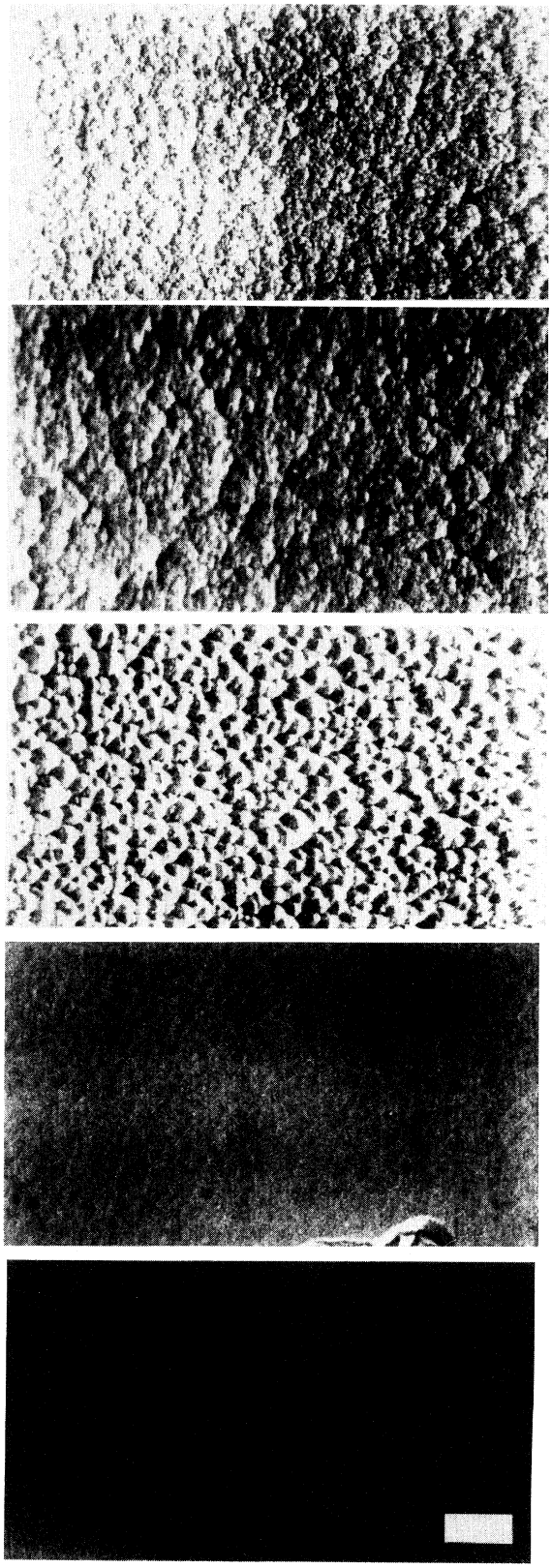

FIG. 10. Scanning electron micrographs of the top interfaces of sputter deposited amorphous germanium. The white bar marker denotes 1 μm.

sponds to an increase in the ion bombardment rate which is the primary mechanism for resputtering [33]. The thermal restructuring of the interface is negligible since the substrate temperature is equal to about one third of the melting point. With the high rate of redistribution after the initial sputtering (lowest photograph) the interface is flat with no structure. The middle photograph shows the tops of the columns that grow vertically upward, while in the top photograph, corresponding to the lowest resputtering rate, the columns grow outwardly, and the top of the film has the characteristic cauliflower morphology. This set of regimes is produced in our simulations on varying the intensity of the incoming rain. The more intense rain effectively corresponds to the lower redistribution rate of the atoms.

Our calculations of nonvertical rain deposition in $d=1+1$ were carried out with constant A_z and A_x mag-

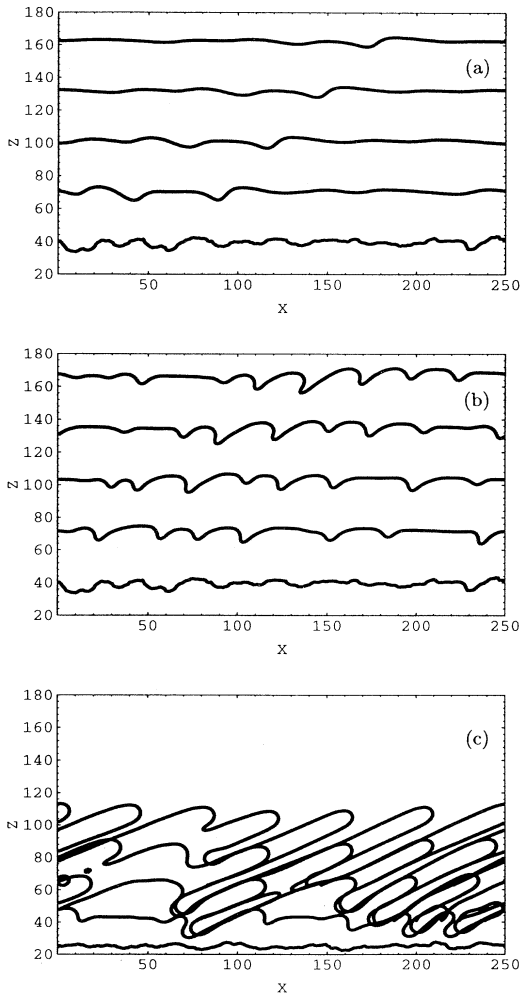

FIG. 11. Snapshots of interfaces $f=0$ taken at $t=100$, 200, and 500, respectively, for off-vertical rain deposition, $g_0 A_z=0.6$; the noise term was operative only until $t=100$. (a) $\gamma=45°$. (b) $\gamma=60°$. (c) $\gamma=75°$.

nitudes chosen to obtain a desired value of $\gamma = \tan^{-1}(A_x/A_z)$ [Fig. 5(b)]. Two distinct morphologies are found: for small values of γ the interfacial geometry is the same as the $\gamma = 0$ case, whereas for large values of γ columnar growth occurs, with the interface being neither a self-affine nor a self-similar fractal. For $g_0 A_z = 0.6$, the crossover from one regime to the other is found to occur at $\gamma_c \simeq 55°$. The columnar structure arises from nonlocal shadowing effects. This transition is shown in Fig. 11. The growth process was initially carried out with the noise term present, then the noise was turned off. Figure 11(a) shows the small γ case in which the interface is smoothened out. Figure 11(b) corresponds to a crossover regime, while Fig. 11(c) for large γ shows a columnar structure. Figure 12(a) illustrates the density profiles of the film for $\gamma = 45°$. The columnar matchstick morphology is qualitatively the same as observed in sputter-deposited films [see Fig. 12(b)]. It also suggests that the transition from self-affine to a periodic columnar structure is not sharp. For $\gamma = 45°$ the interface defined as $f = 0$ does not have a columnar structure even through the interior of the film has already developed a columnar morphology. With increasing γ, zero density gaps are created between the columns. The precise relationship between γ and the growth angle of the structure, γ_G, depends on the strength of the rain, since there are two characteristic time scales in the system set by the strength of the rain and by the diffusional smoothing. A consequence of the competition between these two time scales is shown in Fig. 13. Both panels have a bump in the initial condition and a rain angle of $\gamma = 45°$. For the lower set of curves (a lower intensity of $A_z g = 0.6$), diffusion is able to smooth the interface sufficiently to eliminate the role of shadowing effectively with the overall interface growing at a uniform rate. On the other hand, the upper figures ($A_z g = 2.4$) show not only that γ_G is different from the weaker rain case, but also that the groovelike structure persists at least to the time we

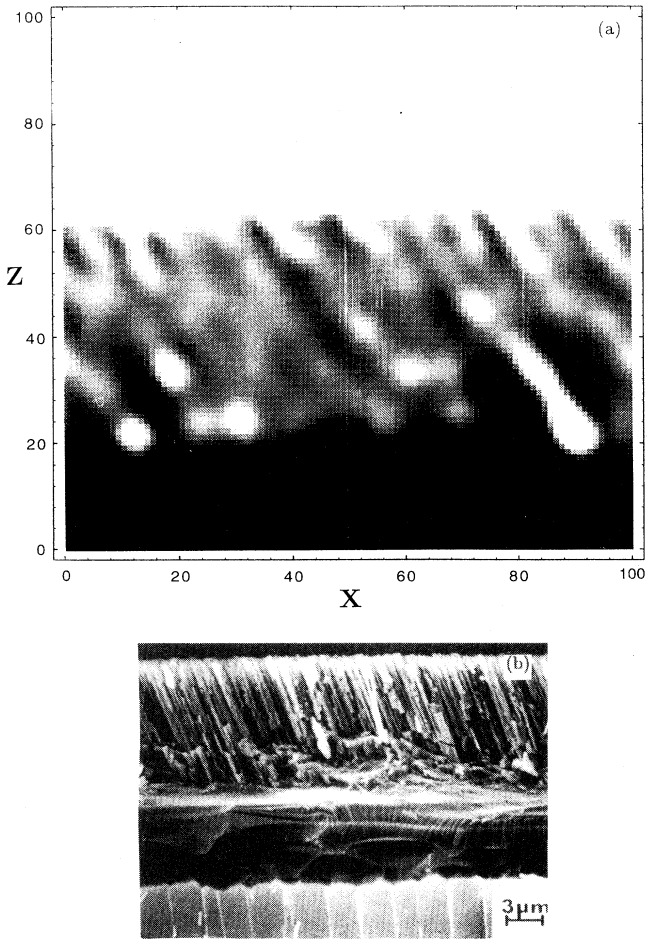

FIG. 12. (a) Density profiles for ballistic flux arriving at angle 45° with respect to the vertical direction on a one-dimensional substrate. Intensity of the flux $g_0|\mathbf{A}| = 4$ and $a = 1$. The white region corresponds to $f = -1$, while the darkest region denotes $f = +1$. (b) Scanning electron micrograph of the cross section of a 20 μm-thick a-Ge film showing the substrate (bottom) and both unetched (middle) and chemically etched morphology (top) revealing the internal, anisotropic density fluctuations. The columnar units are inclined at 20° with respect to the substrate normal.

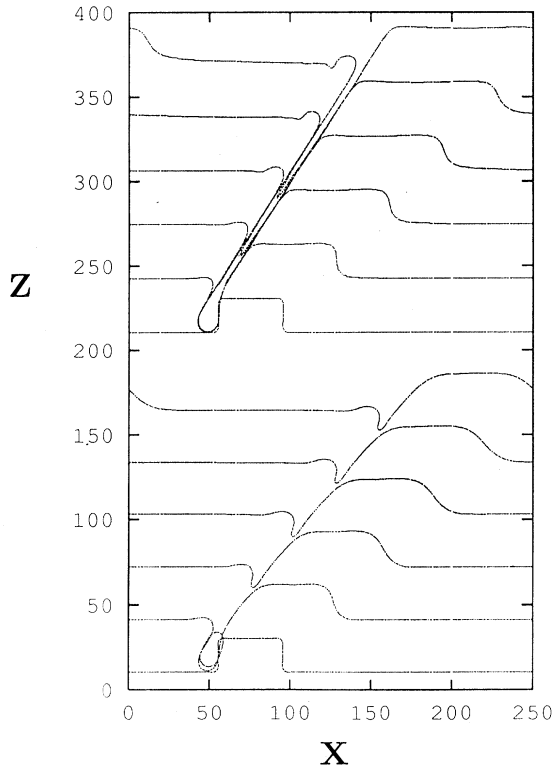

FIG. 13. Growth of a rectangular bump with off-vertical deposition at $\gamma = 45°$. The lower panel shows the sequence of interfaces ($f = 0$) for $g_0 A_z = 0.6$. The noise was turned off for these simulations. The top panel showing the $f = 0$ contour for $g_0 A_z = 2.4$ has been shifted vertically by 200 units for clarity.

have studied. It is important to note that the nonzero value of γ_c arises from the presence of surface tension in the model.

In sputter deposition experiments, the incoming particles have a continuous range of incident angles [6]. In order to mimic this effect in a simplified manner, we have generalized the model to incorporate two incoming rain directions by utilizing two g fields. We choose to study the symmetric case [Fig. 5(c)]. The g fields are noninteracting, and each is converted into the f field independently at the vicinity of the growing interface. In this case, three morphological patterns are observed as γ is varied. The first (for small values of γ) is similar to the vertical rain deposition case. Figure 14(a) illustrates the density profiles of the film for $\gamma=70°$. The matchstick columnar morphology is clearly present, and indeed is qualitatively the same as in the sputter-deposited films when the incidence of the incoming rain is on average vertical [Fig. 14(b)]. For larger values of γ, the interface is characterized by a well-defined length scale—the growth structure consists of columns with deep grooves. Unlike the structure discussed in Sec. II, the columns grow along the vertical symmetry direction (Fig. 15). On increasing γ further, an additional regime is found in which the interface is fractal [Fig. 16(a)] with a fractal dimension of 1.60 ± 0.04 [Fig. 16(b)]. The angles at which the transitions take place are functions of the strength of the rain, as before. The latter transition to the fractal interface (the critical value of γ is around 80° and is only weakly dependent on the strength of the rain) is analogous to that found recently in a different context by Tang and Liang [34]. In the fractal interface regime (large γ), we found the temporal growth exponent $\beta\approx1$ in accord with the visual observation that the pattern grows as a set of independent separated trees with a competition dwindling the number of trees as time evolves.

In summary, in this section we have presented a framework for the study of the growth and morphology of thin films. Our analysis allows for overhanging configurations and is able to accommodate nonlocal shadowing effects. Further, the density profiles of the growing film are straightforwardly obtainable with our model, and are in qualitative accord with experiment. In the simplest case of vertical rain, our results are in accord with those of previous approaches, but underscore the importance of

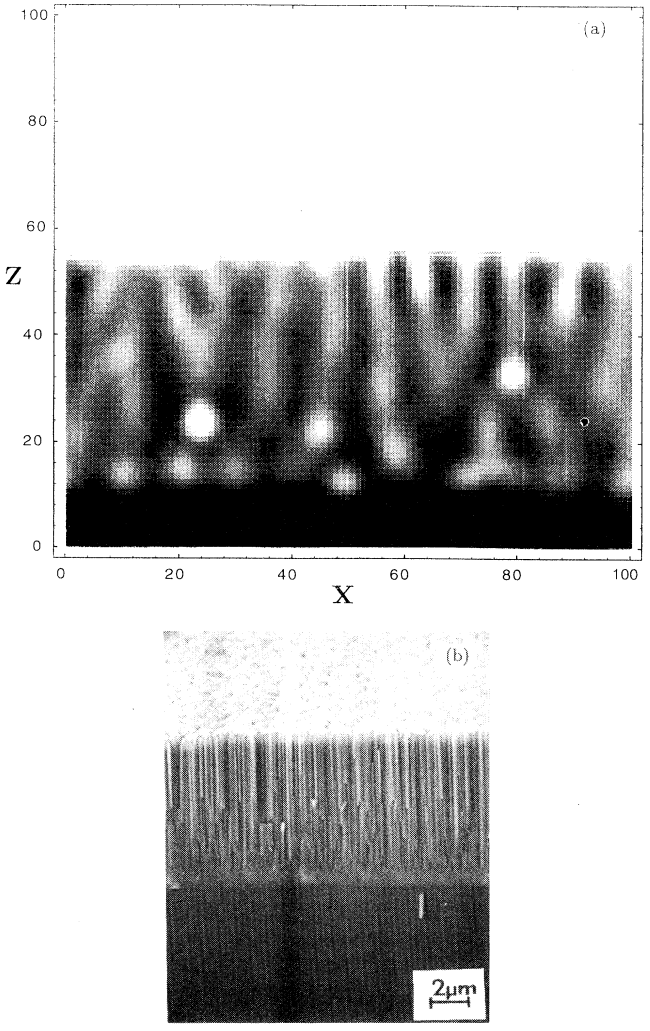

FIG. 14. (a) Same as Fig. 11(a), but with two ballistic fluxes arriving symmetrically toward the interface both at an angle of 70° with respect to the vertical direction ($g_0|\mathbf{A}_1|=g_0|\mathbf{A}_2|=5$). (b) Scanning electron micrograph of a 20-μm-thick film in which the anisotropic columnar morphology (middle) is normal to the substrate surface and parallel to the average incident angle of the depositing vapor species.

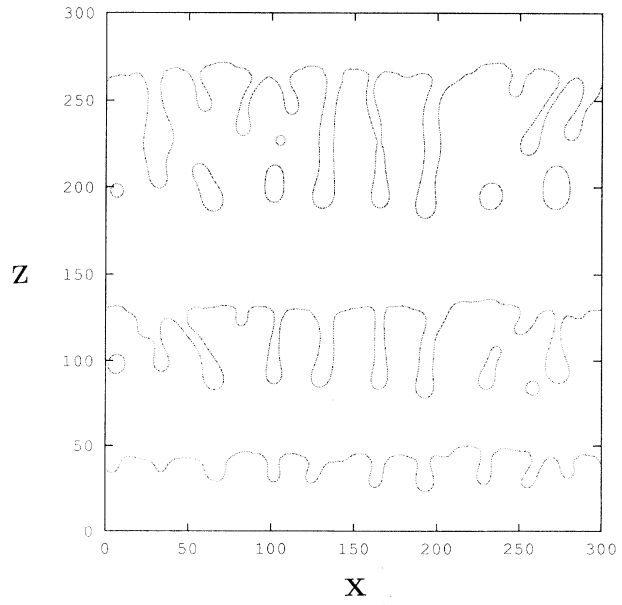

FIG. 15. Snapshots of interfaces $f=0$ taken at $t=300$, 600, and 900, respectively, for two-rain deposition; $\gamma=72°$, and $g_0A_z=0.2$. The contours for $t=600$ and 900 have been shifted vertically by 50 and 150 units, respectively.

allowing for overhanging configurations. For nonvertical rain and when two simultaneous rains occur, a rich range of patterns is observed including a compact, self-affine, and self-similar interface Our model captures *diffusional processes* that are normally ignored in simple simulations, and is a good starting point for detailed studies of the effects of adatom mobility and the geometry of incidence on the structure of thin films.

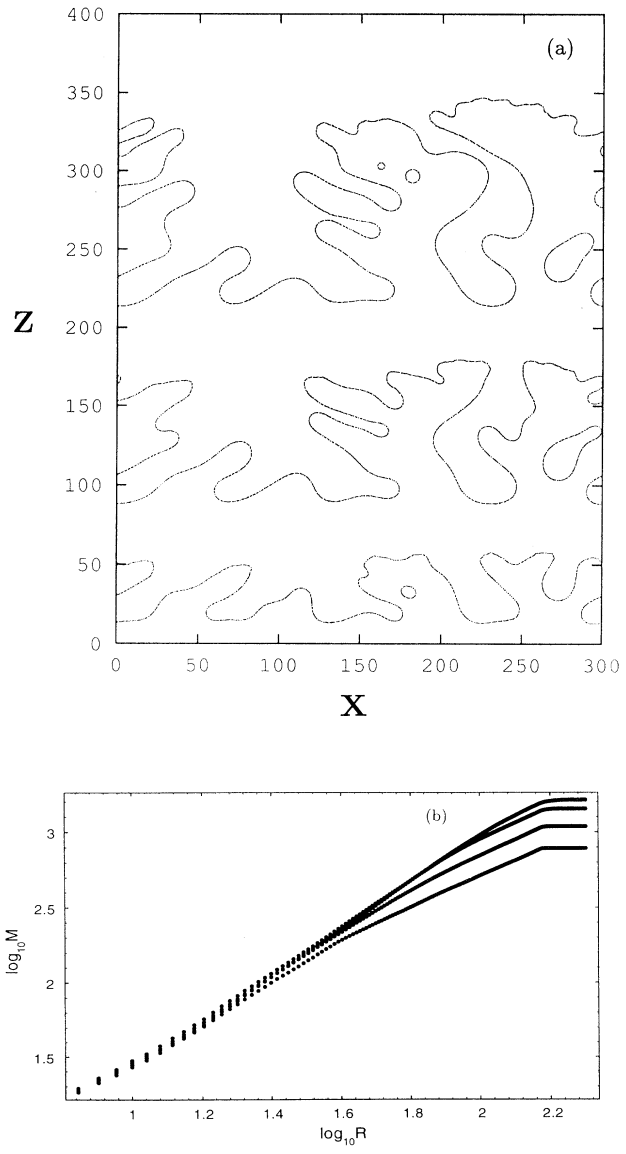

FIG. 16. (a) Same as Fig. 14 but for $\gamma=85°$. Data for $t=600$ and 900 have been shifted by 75 and 200 units vertically. (b) Log-log mass-distance relationship for the systems shown in (a) averaged over ten samples. At later times and longer length scales, there is a fractal regime.

IV. NON-OVERHANG APPROXIMATION

From the point of view of computational efficiency, and to facilitate an analytical analysis, it is often convenient to work within the no-overhang approximation. The position of the interface, h, is defined as a single-valued function of the substrate coordinates. For example, as in $d=1+1$, $h=h(x,t)$. The no-overhang approximation works efficiently as far as overhanging configurations are not important, at least in a large scale limit, and nonlocal effects do not play a role. One may try to incorporate the influence of overhanging configurations by defining the single-valued position of the interface, $h(x,t)$, as the *highest* point of the interface for a substrate coordinate x, and adding appropriate terms to the growth equation. One example is the KPZ equation [24]. The nonlinear term in this equation is able to mimic the faster growth of the high slope regions. In ballistic deposition such a phenomenon arises due to the lower filling of the regions with high slope, since incoming particles in this region stick sidewards to neighboring columns and are thus more likely to produce overhangs. In this section we examine models that attempt to explain the columnar morphology observed in thin films within the no-overhang approximation and relate them to our model [Eqs. (7) and (8); we refer to this model in this section as the f-g model].

First we discuss a model introduced by Mazor *et al.* [30] (see also Sec. III). In order to study the origin of the columnar morphology, they proposed a simple partial differential equation whose linearized version is given by

$$\frac{\partial h(x,t)}{\partial t}=-k\nabla^4 h+\nu\nabla^2 h \ . \tag{9}$$

The $k>0$ term represents the surface diffusion that redistributes particles arriving vertically toward the interface. The $\nu<0$ term mimics the faster growth of the hills ($\nabla^2 h<0$) than of the valleys ($\nabla^2 h>0$) due to the finite size of the particles. The linear stability analysis of Eq. (9) shows that modes with wavelengths $\Lambda>\Lambda_0=(4\pi^2 k/-\nu)^{1/2}$ are unstable, with the fastest growing mode at $\Lambda=\sqrt{2}\Lambda_0$. The nonlinear terms omitted in Eq. (9) saturate these instabilities [30]. Figure 17(a) shows snapshots of interfaces generated from Eq. (9) with $k=1$ and $\nu=-0.1$. The characteristic columnar structure originates from the growth of the most unstable mode.

We now return to the f-g model in which an arbitrary interfacial topology is permitted, and columns are allowed to merge with each other. As in the ballistic deposition model, due to the development of overhangs the high slope regions grow faster, since the density of the aggregate is lower there. These effects may be accommodated within the no-overhang approximation by the presence of the KPZ nonlinear term—$\lambda(\nabla h)^2$. One can modify Eq. (9) by adding the λ term to its right hand side. It is interesting to note that this modification leads to the Kuramoto-Sivasinski (KS) equation [35] that was derived in the context of intrinsic instabilities like flame propagation. Figure 17(b) shows interfaces generated from the modified equation with $k=1$, $\nu=-0.1$, and $\lambda=0.05$. Initially the growth is similar to that in Fig. 17(a). Once

the high slope regions are formed, the nonlinear term causes changes in the growth pattern. Now columns spread, merge, and regenerate. This picture is similar to that obtained in the f-g model (Fig. 7).

Another interesting approach to columnar growth was proposed by Golubovic and Karunasiri [25]. They considered a nonlinear version of Eq. (9) with the noise term present. They showed that even with a positive value of ν, nonlinearities together with the noise term conspire to produce a columnar structure. The interface develops a state which is described by an equation similar to spinodal decomposition. We now extend their model to situations in which the incidence of the incoming flux is oblique. The nonlinear equation for the growth of the interface has a general form [36]

$$\frac{\partial h}{\partial t}=k\sqrt{g}\,\underset{\sim}{\Delta}\frac{\partial S}{\partial h}-\sqrt{g}\,\mathbf{J}\cdot\mathbf{n}\left[1-\tau\frac{\delta S}{\delta h}\right]+\eta\ , \tag{10}$$

where $S=\int dx\sqrt{g}$, with $g=1+(\nabla h)^2$ being the measure of the interfacial area, and $\underset{\sim}{\Delta}=1/\sqrt{g}\,\sum_{i,j=1}^{d}(\partial/\partial x_i)[\sqrt{g}\,g^{ij}(\partial/\partial x_j)]$ is the Beltrami-Laplace operator with $g^{ij}=\delta^{ij}-(1/g)(\partial h/\partial x_i)(\partial h/\partial x_j)$ being the inverse of the metric tensor of the surface. The vector $\mathbf{J}$ represents the incoming flux, and $\mathbf{n}$ is normal to the interface. The k term is responsible for the surface diffusion, whereas the τ term originates from instabilities due to the finite size of the particles. η is a Gaussian noise with zero mean and $\langle\eta(\mathbf{x},t)\eta(\mathbf{x}',t')\rangle=2D\delta^d(\mathbf{x}-\mathbf{x}')\delta(t-t')$.

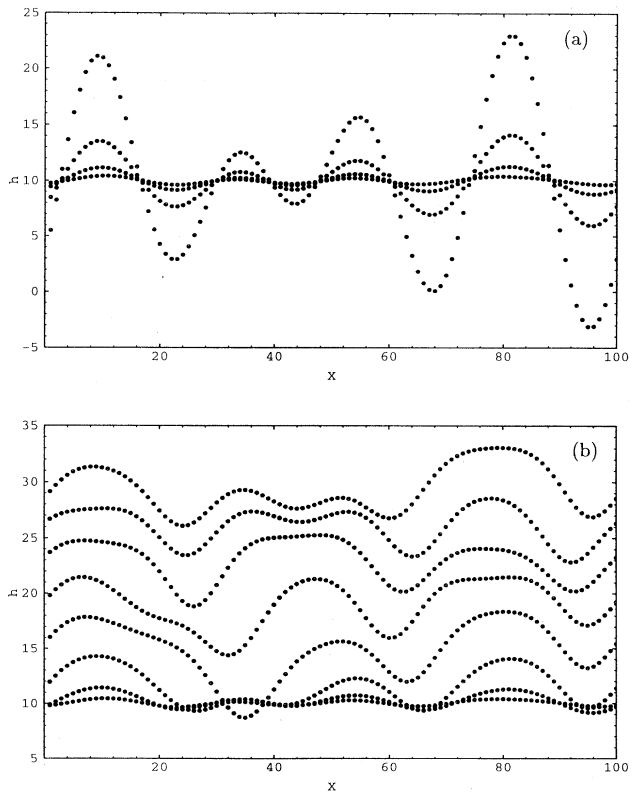

FIG. 17. (a) Interfaces generated from Eq. (9) taken at $t=100$, 200, 300, and 400. Initially the interface was at $h(x,0)=10$ with small random fluctuations added in order to trigger the growth of columnar instabilities. (b) Same as in (a) but with the KPZ nonlinear term added to the right hand side of Eq. (9). Snapshots taken at $t=100, 200, \ldots, 800$.

In $d=1+1$, in the frame of reference that moves upward with the average position of the interface and slides due to the nonzero component of the flux tangential to the interface, $h(x,t)\rightarrow -J_z t+h(x+J_{\parallel}t)$, and Eq. (10) becomes

$$\frac{\partial h}{\partial t}=\tau\left[J_z-J_{\parallel}\frac{\partial h}{\partial x}\right]K-k\frac{\partial}{\partial x}\left[\frac{1}{\sqrt{g}}\frac{\partial}{\partial x}K\right]+\eta(x,t)\ , \tag{11}$$

where $J_z<0$ and $J_{\parallel}$ are the vertical and tangential components of the flux, respectively, and $K=(\partial/\partial x)[(\partial h/\partial x)/\sqrt{g}\,]$, with $g=1+(\partial h/\partial x)^2$ being the curvature of the interface.

Following Golubovic and Karunasiri, we change the variables into $m=\partial h/\partial x$. Equation (11) maps into

$$\frac{\partial m}{\partial t}=(\partial_x)^2F(m)+\frac{\partial\eta}{\partial x} \tag{12}$$

with

$$F(m)=-k\left[\frac{(\partial_x)^2m}{(1+m^2)^2}-\mu\frac{m(\partial_x m)^2}{(1+m^2)^3}\right]+\tau\frac{\partial}{\partial m}(J_z\sqrt{1+m^2}+J_{\parallel}\sinh^{-1}m)\ , \tag{13}$$

where the parameter $\mu=3$ is introduced for convenience. Assuming that changing $\mu=3$ into $\mu=2$ does not crucially change the physics described by Eq. (11), Eq. (12) can be rewritten as

$$\frac{\partial m}{\partial t}=(\partial_x)^2\frac{\delta H}{\delta m}+\frac{\partial\eta}{\partial x} \tag{14}$$

with

$$H(m)=\int dx\left[\tau(J_z\sqrt{1+m^2}+J_{\parallel}\sinh^{-1}m)+\frac{k}{2}\frac{(\partial_x m)^2}{2(1+m^2)^2}\right]\ . \tag{15}$$

Equations (14) and (15) describe model B [26] conserved order parameter dynamics which is extensively used in the study of the spinodal decomposition process. The steady state distribution of Eq. (14) is governed by the Boltzman factor $\exp[-H(m)/D]$. The corresponding partition function is

$$Z=\prod_x\int_{-\infty}^{\infty}dm(x)\exp[-H(m)/D]\ . \tag{16}$$

With the change of variables $m(x)=\tan\Theta(x)$, and assuming that the noise in Eq. (11) is short range correlated

with a cutoff length for fluctuations equal to a, the partition function maps into

$$Z=\prod_x \int_{-\pi/2}^{\pi/2} d\Theta(x)\exp[H_{\rm eff}(\Theta)/D] \tag{17}$$

with

$$H_{\rm eff}(\Theta)=\int dx \left\{ \tau \left[\frac{J_z}{\cos\Theta(x)} + J_\parallel \ln\left[\frac{1+\sin\Theta(x)}{\cos\Theta(x)} \right] \right] + \frac{k}{2}[\partial_x \Theta(x)]^2 + \frac{2D}{a}\ln[\cos\Theta(x)] \right\} . \tag{18}$$

Even though the coefficient τJ_z is negative, gravitational effects or the condensation-evaporation process can effectively change the sign of this coefficient. The $\tau J_\parallel$ coefficient breaks the inversion symmetry, $x \to -x$, and is not influenced by the above phenomena since they preserve this symmetry. Assuming that τJ_z is positive with $J_\parallel = 0$, we reobtain the Golubovic-Karunasiri results: If $\tau J_z > 2D/a$, $H_{\rm eff}$ has a single minimum at $\Theta = 0$. The presence of the $J_\parallel$ term simply shifts the minimum to $\Theta \neq 0$. If $\tau J_z < 2D/a$, $H_{\rm eff}$ has two minima at the two symmetric values $\Theta_\pm = \pm \tau J_z / 2D/a$ [see Fig. 18(a)]. When $J_\parallel \neq 0$, one minimum is lowered while the other is shifted up [see Fig. 18(b)]. Thus $J_\parallel$ is akin to a magnetic field.

We have confirmed this observation by a numerical solution of Eq. (11). The details of the calculation are similar to that in Ref. [25]. We generate a short-range-correlated noise by eliminating short wavelength components of an uncorrelated Gaussian noise with the use of the fast Fourier transform (FFT). We choose the noise strength $D = 0.1$, cutoff length for fluctuations $a = 3$, and the coefficient $k = 1$. It was estimated in Ref. [25] that with these conditions the transition occurs at $\tau J_z \sim 0.03$. Figure 19(a) shows the evolution of the probability distribution function of $\Theta(x,t)$ and $P(\Theta)$, for $\tau J_z = 0.01$ and $J_\parallel = 0$. The system is in the two phase region. Initially, $P(\Theta)$ has a single maximum that spreads and finally splits into two symmetric maxima. Figure 19(b) shows an evolution similar to the one in Fig. 18(a), but with the oblique flux term $\tau J_\parallel$ present. Initially, the evolution is the same as before. However, at late stages $P(\Theta)$ shows two unequal maxima. This is in accord with the analysis we have presented above. The higher and lower maxima in $P(\Theta)$ correspond to the lower and higher minima, respectively, in $H_{\rm eff}(\Theta)$.

The shape of $P(\Theta)$ with an oblique flux present corresponds to the columnar structure of the interface with the column walls being steeper on the side exposed to the flux. It is in qualitative accord with the results obtained in the f-g model. Figure 11(b) shows such a situation. Overhanging configurations are not present, and the steep parts of the interface exposed to the rain can be observed. However, the no-overhang approximation breaks down when shadowing effects become important. Figure 11(c) shows a columnar structure with overhangs present. The columnar walls are essentially shadowed from the growth and only the column tops are exposed to the rain. The direction of the growth is different from that of the flux while in the no-overhang approximation they are the same.

In this section, we have discussed models for columnar morphology within the no-overhang approximation. Such an approach is able to elucidate the origin of the initial instabilities that lead to the development of columns. When the influence of the overhangs is only local, the nonlinear KPZ term captures the essential features of the growth. We have shown that this approximation is also able to capture the main trends in the pattern changes due to an oblique incident flux. The no-overhang approximation breaks down when nonlocal effects become important. Examples include the development of outward flaring columns in the presence of intense vertical rain (see the inset in Fig. 7), inclined columnar structures observed when an incident incoming flux of sufficient strength makes a large angle with the normal to the substrate, and the set of patterns observed in the f-g model when the incoming rain is no longer unidirectional.

V. DIFFUSION-LIMITED AGGREGATION

A number of growing structures ranging from viscous fingering, solidification of an undercooled liquid, dielectric breakdown, chemical dissolution, and electrodeposition have striking similarities [10-18]. They all originate within a unified framework of the diffusion-limited-aggregation (DLA) process. The discrete version of DLA was proposed by Witten and Sander [10]. In their model, the aggregating particles move randomly one at a time, and at the first encounter deposit on the aggregate. A

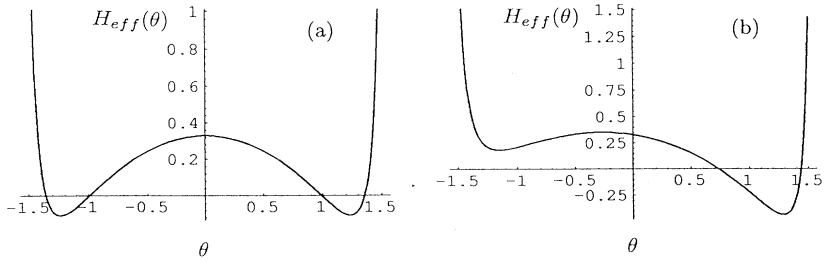

FIG. 18. Plot of $H_{\rm eff}$ as a function of Θ given by Eq. (18) in the $0 < \tau J_z < 2D/a$ regime. (a) $J_\parallel = 0$. (b) $J_\parallel \neq 0$.

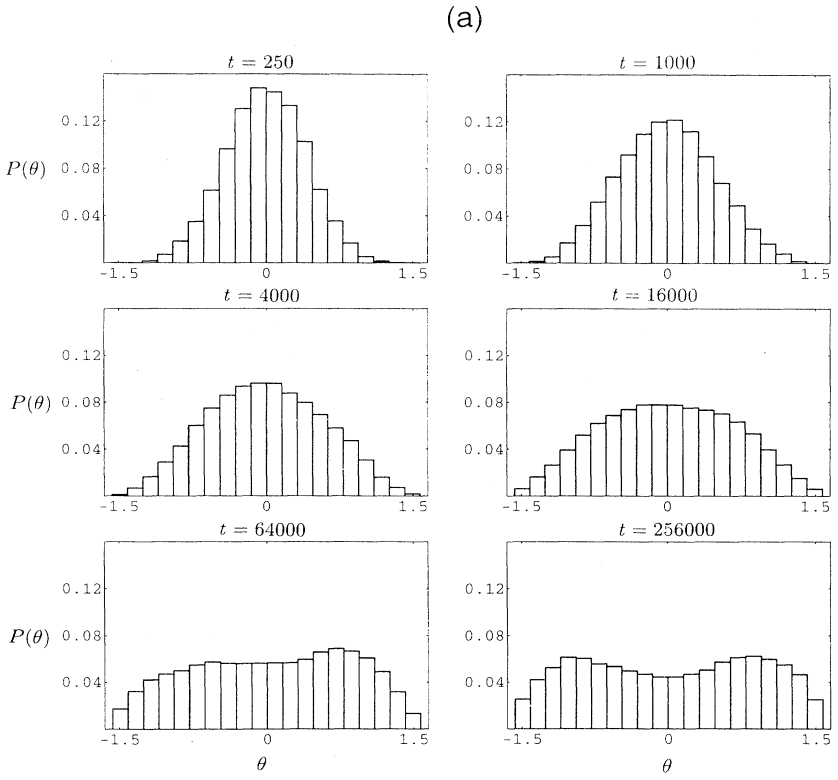

FIG. 19. (a) Evolution of $P(\Theta)$ for Eq. (11) with $\tau J_z = 0.01$ and $\tau J_\parallel = 0$. Plots have been obtained by dividing the interval $[-\pi, \pi]$ into 20 equals bins, and by counting the number of sites x for which $\Theta(x)$ belongs to a given bin. $P(\Theta)$ is normalized in such a way that the sum over bin heights is equal to 1. Data are for lateral size 2048, averaged over five samples. (b) Same as (a), but with $J_\parallel = 0.005$.

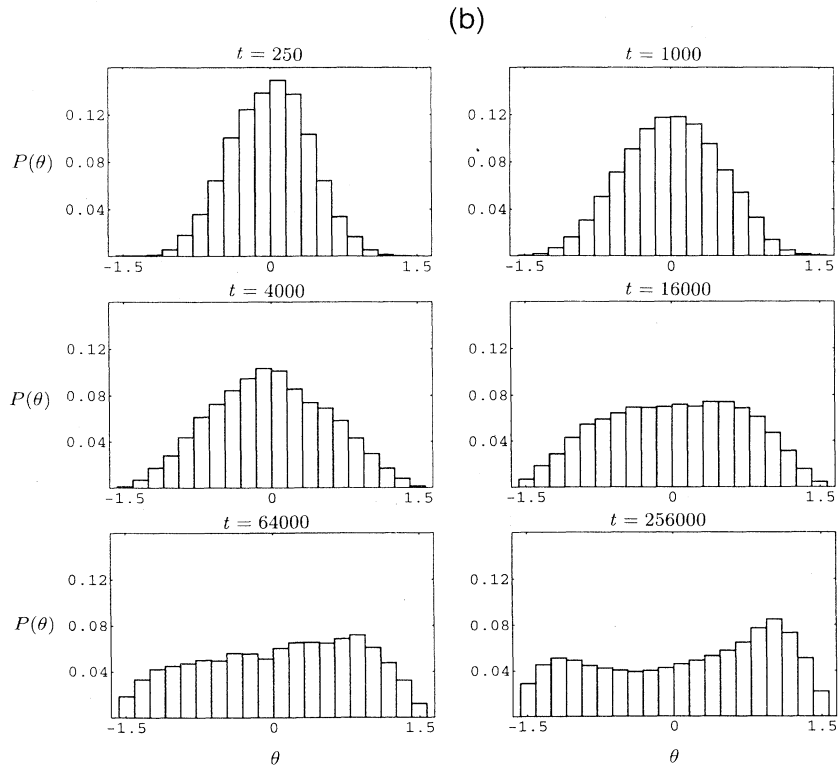

number of modified versions of this process with different attachment procedures have been developed. In a continuum version of the problem, one needs to solve Laplace's equation—a steady state limit of the diffusion equation—with suitable boundary conditions. The growth rate is taken as being proportional to the gradient of the field at the interface, which represents the incoming flux of the particles toward the interface [11,37]. Both techniques require the monitoring of the interface. In the discrete problem, one needs to know when the particle touches the aggregate. In the Laplacian approach the boundary conditions are defined at the interface.

It is straightforward to modify the model presented in Sec. III to include DLA-type phenomena within its description. We have already developed the machinery for both an arbitrary topology of the interface with its dynamics and the way to incorporate the dynamics of the aggregating vapor. We just need to substitute the ballistic flux with a diffusive flux that is responsible for the transport of the aggregating field.

Our equations are modified to

$$\frac{\partial f(\mathbf{r},t)}{\partial t}=\nabla^2\frac{\delta F}{\delta f(\mathbf{r},t)}+J(\mathbf{r},t)\ , \tag{19}$$

$$\frac{\partial g(r,t)}{\partial t}=D\nabla^2 g(\mathbf{r}t)-J(\mathbf{r},t)\ . \tag{20}$$

The first part of Eq. (19) and the free energy F is the same as that described previously. The interaction term $J>0$ leads to the growth of f and decay of g such that $f+g$ is a conserved quantity, and changes only due to the sources of the g field at the boundary. To simulate different experimental situations we studied two interaction mechanisms [38],

$$J_1(\mathbf{r},t)=-\nabla f\cdot D\nabla g\cdot\eta(\mathbf{r},\mathrm{t}) \tag{21}$$

and

$$J_2(\mathbf{r},t)=D_2\cdot g|\nabla f|^2\cdot\eta(\mathbf{r},t)\ , \tag{22}$$

where $\eta(\mathbf{r},t)$ is a Gaussian noise with a nonzero average value $V>0$ and width W. For the planar geometry the initial and the boundary conditions for f are the same as for ballistic deposition calculations. The g field initially was chosen to be $g(z)=g_0 z/z_u$ for $f<0$, and $g=0$ for $f>0$, where z_u is the position of the upper boundary with the $f=0$ interface located at $z=0$. During simulation we kept g at the upper boundary constant, or alternatively we varied g at the boundary to maintain a constant flux $-D\nabla g$. We also carried out circular geometry simulations for growth starting from an initial seed located at the middle of the sample and the g field arriving from the edges of the system.

The physics of the aggregation again relies on the conversion of the g field into the f field which causes the $f=+1$ regions to grow, thereby advancing the $f=0$ interface. The g field is transported by the diffusive flux $-D\nabla g$ toward the interfacial region where the conversion occurs. After the conversion, the surface tension built into Eq. (19) redistributes the aggregated g field. Due to the ∇f factor, the J_1 and J_2 terms are operative only in the interfacial region. They are the source of growth of the f field. The J term with negative sign in Eq. (20) takes into account the removal of the g field. The $-D\nabla g$ factor in the J_1 growth term represents the analog of boundary conditions of the Laplacian solution and ensures that the aggregation rate is proportional to the incoming flux magnitude. Thus we implement dynamically the condition of g being zero at the interface, which we shall show leads to typical DLA growth patterns. The J_2 growth term is proportional to the g field density itself and leads to g being nonzero at the interface and allows for a diffusive flux with a nonzero component tangential to the interface.

Our approach is similar to the phase field model [39] where two coupled differential equations are used to describe the solidification process of an undercooled liquid. In that case, one field describes the temperature and the other phase field is used to characterize the solid and liquid phases [40]. In a context somewhat more similar to the present work, several authors [41] have studied coupled differential equations to monitor the dynamics of the growth process. In all aggregation models, the sum of the diffusive and aggregating fields (f and g) is conserved. The noninteractive part of the phase field equation is nonconservative—both solidification and melting are allowed. In contrast, in our model aggregation is unidirectional. Our model decouples the surface diffusion process from the conversion process, and aggregated par-

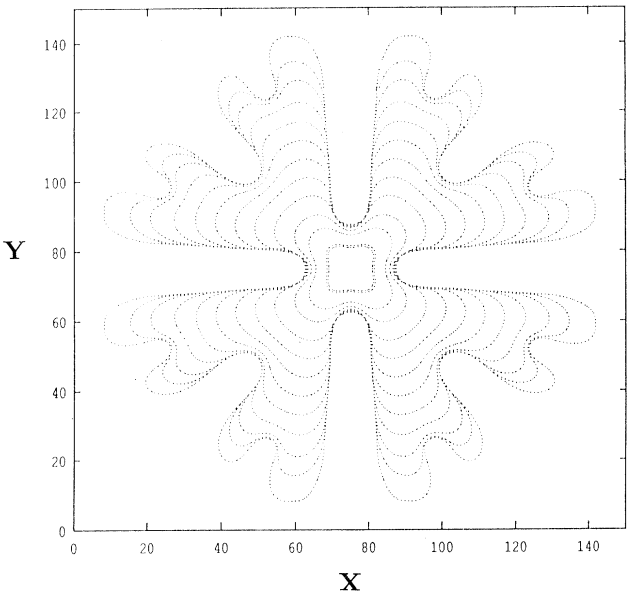

FIG. 20. Sequence of interfaces (defined as $f=0$) for growth from small square located at the center of the sample using the J_1-interaction mechanism. The noise width W is set to zero, and g is held fixed temporally in an inhomogeneous manner on the square boundary of the figure, so that initially $\nabla^2 g\equiv 0$ with $g(r=75)=0.5$ and $g(r=5)=0$. The surface tension term $a=\frac{1}{2}$.

ticles are redistributed via conserved dynamics.

We performed our simulations for both planar and circular geometry. Details of the simulations are the same as discussed previously. For computational ease, the interaction was restricted to the $|\nabla f| < 0.8$ region, and the remnants of the g field ($<2\%$) were converted into f in the $f > 0.8$ region.

First we utilize the J_1 growth mechanism. Figure 20 shows a typical pattern in the absence of noise in a circular geometry, which is indeed similar to structures obtained in conventional Laplacian growth [42]. While the initial square symmetry is destroyed by an infinitesimal noise term, finger splitting is operational even without the noise. The typical fingering instability is shown in Fig. 21(a). We studied the Fourier spectrum of the growing interface, confirming the exponential growth of the unstable modes with the growth rate depending on the wave vector approximately in the form proposed by Mullins and Sekerka [43]. In Fig. 21(b) late stages of growth for planar geometry are presented. Successive splittings of the fingers in order to maintain a characteristic finger width, screening of the lower branches by higher ones, and the development of an intricate treelike pattern are discernible in the figure.

The principal length scale introduced by the surface tension parameter is proportional to $\sqrt{a}$. By rescaling Eqs. (19) and (20) one can see that this is an exact statement, although we also verified this result numerically. The characteristic width of the fingers also depends on the boundary flux rate. We find that size of the fingers decreases with increasing flux approximately as the $(\text{flux})^{-1/2}$ [44]—our measurements give an exponent 0.45 ± 0.05. This is simply the consequence of the fact that the flux rate is a measure of the inverse time allowed for the diffusional relaxation. Despite the finger width dependence on the flux rate, we found the fractal dimension remains unchanged from the one obtained in lattice simulations of DLA. This is particularly interesting, since it is known that in solidification processes the scaling of the growth velocity depends on the nature of the cutoff length scale [45]. From this point of view our model is more akin to a diffusion transition model [46]. However, in solidification, undercooling occurs globally in the liquid phase, while our model involves diffusion of the particles from the boundary.

Figure 22(a) shows a typical pattern obtained in circular geometry which is convenient for the measurement of the fractal dimension. A power law mass-radius dependence leads to a fractal dimension equal to 1.65 ± 0.05 [see Fig. 22(b)], which is similar to the value obtained in standard lattice DLA simulations. When the value of g is initially higher, the Laplacian solution is no longer valid—the growth is so rapid that the diffusive field is unable to adjust to the quasistationary solution. Figure 23 shows a cluster with a higher filling than the one resulting from a lower g field density. It is not possible to

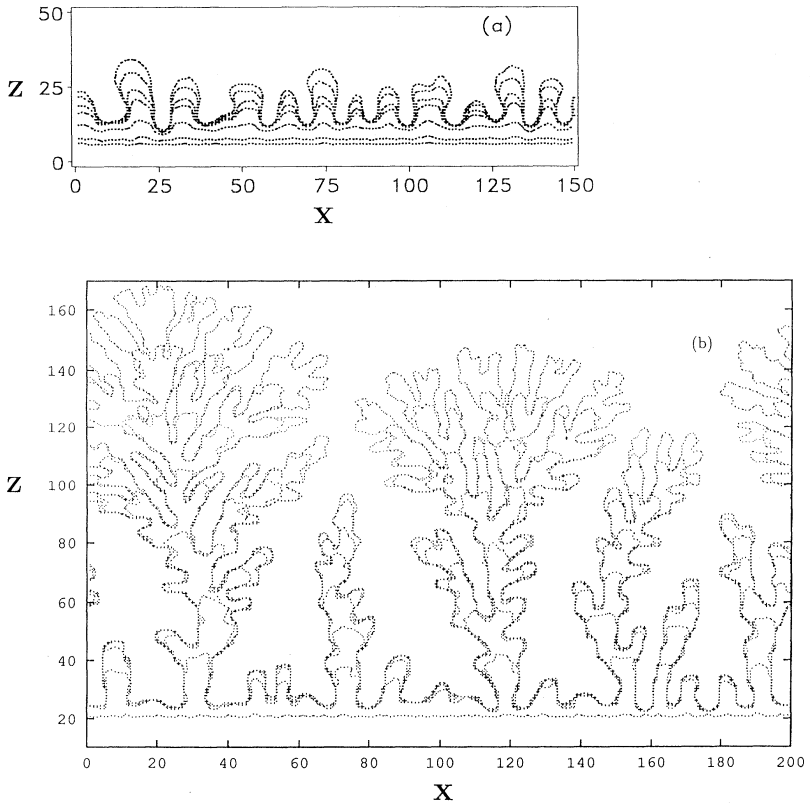

FIG. 21. (a) Initial stages of growth starting from a plane interface with the J_1 mechanism. $a = \frac{1}{4}$. $W/V = \frac{1}{4}$. The flux of the g field was held constant during the simulation. (b) Late stages of growth of the system similar to that shown in (a).

deduce the fractal dimension in this case. At a short length scale, the effective fractal dimension is higher than before, while at a large length scale the effective fractal dimension seems to increase further. This is not unexpected since the density of random walkers is effectively nonzero, contrary to conventional lattice DLA simulations where the random walker density is zero.

In electrochemical deposition experiments, when the rate of deposition is very slow, the local growth effects compete with nonlocal Laplacian effects [18]. With a higher current density the patterns resemble a typical DLA structure, while with low current density a characteristic columnar morphology is observed—there is no side branching, and crevices between the columns are narrow. The physical reason for this is that at low current densities the deposition is slowed down by the potential barrier of water dipole molecules inhibiting the activation of cations in the interface region. The growth rate then would be expected to be proportional to the density of the g field rather then to the flux. This mechanism is captured by the J_2 growth form. Figure 24 shows fingering that bears a striking resemblance to the experimental one—the fingers are much wider than those in Fig. 21(a) and the crevices are narrower. The g field is no longer zero at the interface, and is higher where the growth rate is larger. This causes a diffusion component parallel to the interface to fill the voids between the columns. This effect can be accentuated by *repelling* the g field from the interface (as in the experiment), thus slowing the growth rate and allowing tangential diffusion to smooth the interface. We confirmed this by simulation where Eq. (19) was replaced by

$$\frac{\partial g(\mathbf{r},t)}{\partial t}=\nabla\cdot(D\nabla g+Ag\nabla f)-J_2(\mathbf{r},t)\ . \tag{23}$$

Here the diffusive flux $-D\nabla g$ is complemented with a force-biased flux $-Ag\nabla f$. The ∇f vector is normal to the interface directed towards the $f=+1$ aggregate region and is present only in the vicinity of the interface. For a high magnitude of the repulsive force, the neighboring fingers merge leaving holes behind (Fig. 25) and eliminating DLA-type instabilities. The pattern obtained in this regime is strikingly similar to experimental structures for low current densities [18].

In this section we have utilized our model to describe DLA-type phenomena. In the limit of a low density of random walkers our model is in an agreement with the

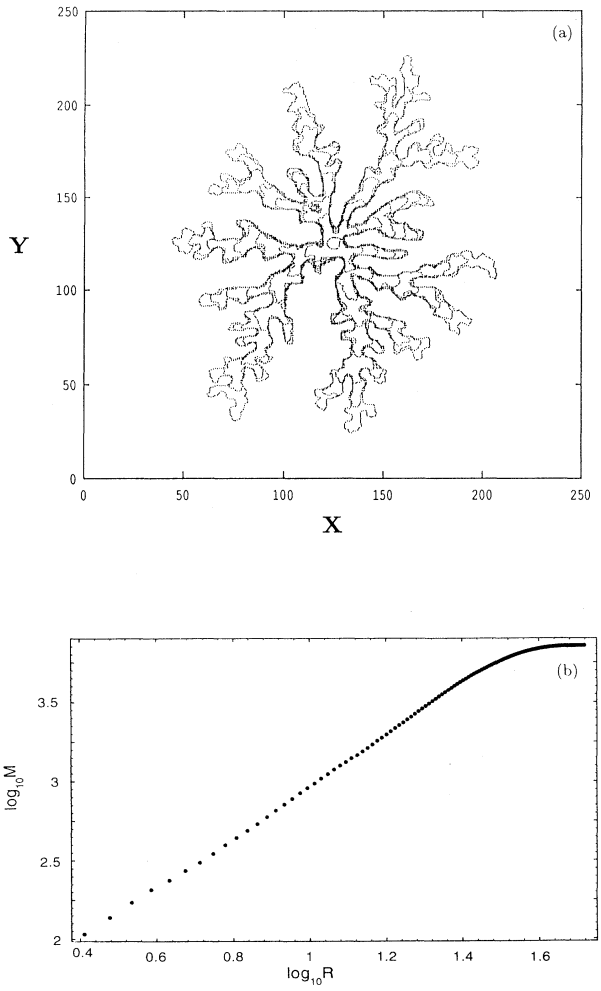

FIG. 22. (a) Circular geometry growth with the J_1 interaction mechanism. At $t=0$, $g(r=125)=\frac{1}{2}$, $g(r=3)=0$, $a=\frac{1}{8}$, and $W/V=\frac{1}{4}$. The boundary condition is as in Fig. 19. (b) Log-log plot of a radius-mass relationship for the systems shown in (a) averaged over ten samples.

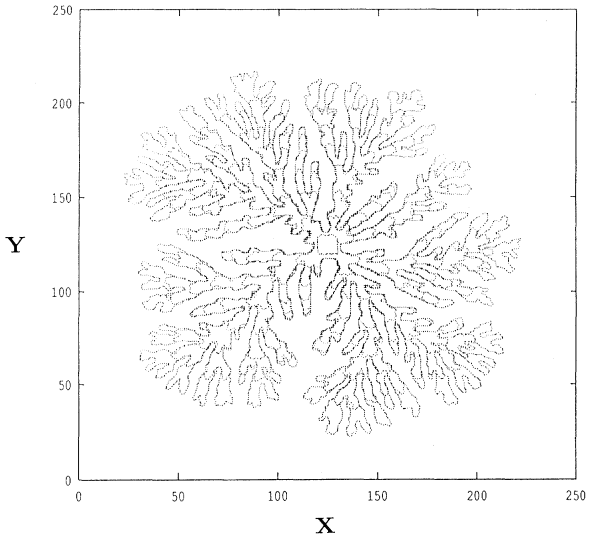

FIG. 23. Same as Fig. 21(a), except $g(r=125)=1$.

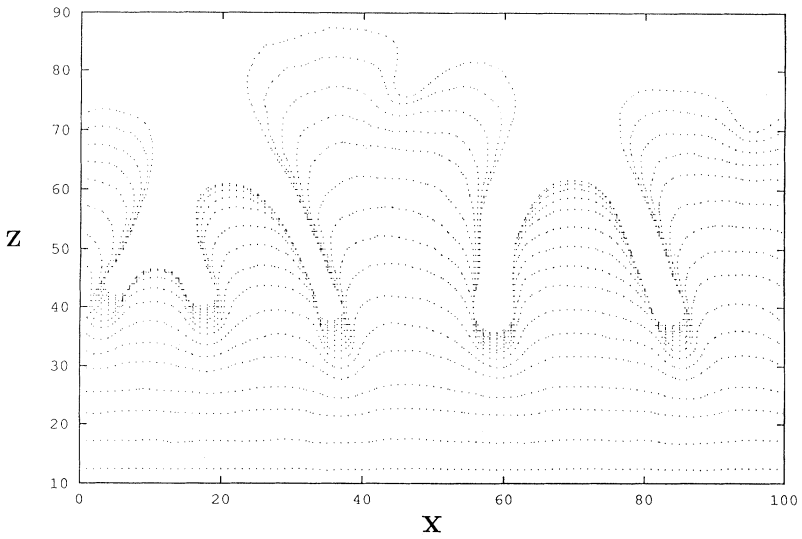

FIG. 24. Initial stages of growth starting from a plane interface with the J_2 mechanism. $a=\frac{1}{4}$ $W/V=1$. The flux of the g field at the boundary was held constant during the simulation.

standard DLA or Laplacian growth model. Our description is able to incorporate surface tension, and a nonzero density of random walkers in a natural manner. A straightforward modification allows the study of situations in which particles interact with the aggregate as in electrodeposition experiments.

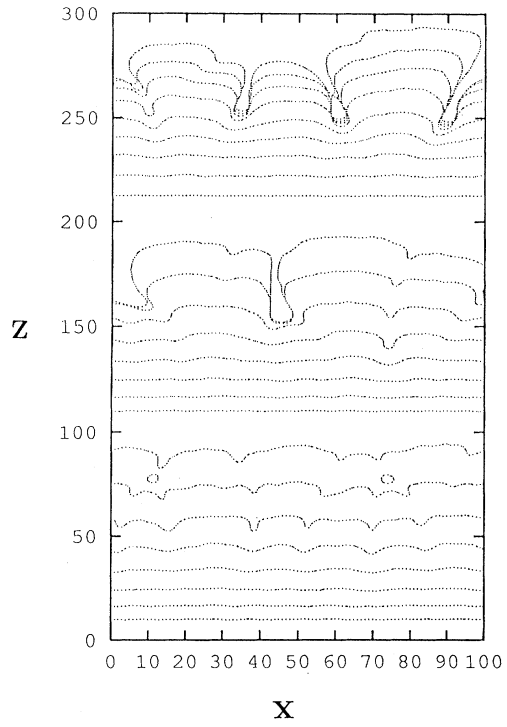

FIG. 25. Same as Fig. 23, but with an additional force repelling the diffusive particles from the growing aggregate [Eq. (23)]. The three panels show the effect of increasing the force magnitude (the force is highest for the bottom panel). The vertical coordinates of the middle and top panels have been shifted by 100 and 200 units, respectively.

ACKNOWLEDGMENTS

We are indebted to Joel Koplik for fruitful collaboration in the earlier stages of this work, and to Shoudan Liang for stimulating discussions. This work was supported by grants from EPSRC, INFM, INFN, NASA, NATO, NSF, ONR, the Donors of the Petroleum Research Fund administered by the American Chemical Society, and the Center for Academic Computing at Penn State.

APPENDIX

In this appendix we will show the nonconserved form of Eq. (2), with the I_1 growth mechanism, i.e.,

$$\frac{\partial f(\mathbf{r},t)}{\partial t}=\Gamma\frac{\partial F}{\partial f(\mathbf{r},t)}+C_1|\nabla f|+D_1\eta(\mathbf{r},t)\ . \tag{A1}$$

where

$$F=\int\left[-\frac{1}{2}f^2+\frac{f^4}{4}+a(\nabla f)^2\right]dv$$
$$\equiv\int[V(f)+a(\nabla f)^2]dv \tag{A2}$$

is indeed equivalent to the KPZ equation for the description of the interface evolution, at least in the limit of small a.

To this end, we follow Bausch *et al.* [47], write $\mathbf{r}\equiv(\mathbf{R},z)$, and decompose $f(\mathbf{R},z,t)$ into two parts:

$$f(\mathbf{R},z,t)=\mathcal{M}\left[\frac{1}{\sqrt{a}}\frac{z-h(\mathbf{R},t)}{\sqrt{1+|\nabla h|^2}}\right]+\mathcal{N}(\mathbf{R},z,t)\ , \tag{A3}$$

where $\mathcal{M}(x)=\tanh(x)$ is the kink solution satisfying

$$\mathcal{M}''+dV(\mathcal{M})/d\mathcal{M}=0\ , \tag{A4}$$

with antiperiodic boundary conditions $\mathcal{M}=\pm1$ as $x\to\pm\infty$. $h(\mathbf{R},t)$ describes the fluctuations of the interface, while $\mathcal{N}(\mathbf{R},z,t)$ contains all fluctuations of f not included in h.

After a change of variables $\mathbf{R}\rightarrow\mathbf{R}'$, $1/\sqrt{a}\,(z-h(\mathbf{R},t))/(\sqrt{1+|\nabla_{\mathbf{R}}h|^2})\rightarrow s$, in the limit of small a we may write Eq. (A1) as

$$\frac{1}{\sqrt{a}}\frac{\dot{h}}{\sqrt{g}}\mathcal{M}'=\frac{\Gamma}{a}[\mathcal{M}''+dV(\mathcal{M})/d\mathcal{M}]-\frac{\Gamma}{\sqrt{a}}\frac{\nabla_{\mathbf{R}}^2 h}{\sqrt{g}}\mathcal{M}'+\frac{\Gamma}{\sqrt{a}}\frac{\nabla_{\mathbf{R}}f\cdot\nabla_{\mathbf{R}}g}{\sqrt{a}}(s\mathcal{M}''+\mathcal{M}')-\frac{C_1}{\sqrt{a}}\mathcal{M}'-\frac{D_1}{a^{1/4}}\mathcal{M}'\frac{\eta(\mathbf{R},z,t)}{g^{1/4}}+O(a^0)\,, \tag{A5}$$

where $g=1+\nabla_{\mathbf{R}}^2 h$.

The first term on the right-hand side is zero due to Eq. (A4). To project out all fluctuations not included in h, we multiply both sides by $\mathcal{M}'$ and integrate over ds [47], and obtain

$$-\frac{\dot{h}}{\sqrt{g}}=\Gamma\left[\frac{\nabla_{\mathbf{R}}^2 h}{\sqrt{g}}-\frac{\nabla_{\mathbf{R}}h\cdot\nabla_{\mathbf{R}}\ln g}{2\sqrt{g}}\right]+C_1+\frac{D_1\theta(\mathbf{R},t)}{g^{1/4}}\,, \tag{A6}$$

where $\langle\theta(\mathbf{R},t)\theta(\mathbf{R}',t')\rangle=2\delta(\mathbf{R}-\mathbf{R}')\delta(t-t')$.

Notice that this is the reparametrization invariant [48] equation whose leading term in $\nabla_{\mathbf{R}}^2 h$ leads to the KPZ equation.

[1] *Dynamics of Fractal Surfaces,* edited by F. Family and T. Vicsek (World Scientific, Singapore, 1991), and references therein; L. A. Barabasi and H. E. Stanley, *Fractal Concepts in Interface Growth* (Cambridge University Press, Cambridge, 1995) and references therein; T. Halpin Healy and Y. C. Zhang, Phys. Rep. **254**, 415 (1995).

[2] For a review of growth involving nonlocal effects, see G. S. Bales, R. Bruinsma, E. A. Eklund, R. P. U. Karunasiri, J. Rudnick, and A. Zangwill, Science **249**, 264 (1990), and references therein.

[3] B. A. Movchan and A. V. Demchishin, Fiz. Met. Metall. **28**, 653 (1969) [Phys Met. Metall. (USSR) **28**, 83 (1969)].

[4] L. R. Gilbert, R. Messier and R. Roy, Thin Solid Films **54**, 149 (1978); R. Messier, S. V. Krishnaswamy, L. R. Gilbert, and P. Swab, J. Appl. Phys. **51**, 1611 (1980).

[5] R. Messier and J. E. Yehoda, J. Appl. Phys. **58**, 3739 (1985).

[6] R. Messier, J. Vac. Sci. Technol. A **4**, 490 (1986).

[7] K. H. Muller, Surf. Sci. Lett. **184**, L375 (1987).

[8] J. Bartholomeusz, K. H. Muller, and M. R. Jacobson, Proc. SPIE **821**, 2 (1987).

[9] J. E. Yehoda, B. Yang, K. Vedam, and R. Messier, J. Vac. Sci. Technol. A **6**, 1631 (1988).

[10] T. A. Witten and L. M. Sander, Phys. Rev. Lett. **47**, 1400 (1981).

[11] For a review see, e.g., Fractals in Physics, edited by L. Pietronero and E. Tosatti (North-Holland, Amsterdam, 1985).

[12] L. M. Sander, Nature **332**, 789 (1986).

[13] J. Nittamann and H. E. Stanley, Nature **321**, 663 (1986).

[14] L. Paterson, Phys. Rev. Lett. **52**, 1621 (1984).

[15] J. Nittamann, G. Daccord, and H. E. Stanley, Nature **314**, 141 (1985); T. Maxworthy, Phys. Rev. A **39**, 5863 (1989).

[16] E. Ben-Jacob *et al.*, Phys. Rev. Lett. **55**, 1315 (1985).

[17] L. Neimeyer, L. Pietronero, and H. Weisman, Phys. Rev. Lett. **52**, 1033 (1984).

[18] G. L. M. K. S. Kahanda, X. Zou, R. Farrel, and P. Wong, Phys. Rev. Lett. **68**, 3741 (1992).

[19] P. Meakin, CRC Crit. Rev. Solid State Sci. **13**, 143 (1987), and references therein.

[20] See, e.g., G. H. Gilmer and M. Grabow, Proc. SPIE **821**, 56 (1987).

[21] P. Keblinski, A. Maritan, F. Toigo, J. Koplik, and J. R. Banavar, Phys. Rev. E **49**, R937 (1994).

[22] P. Keblinski, A. Maritan, F. Toigo, and J. R. Banavar, Phys. Rev. E **49**, R4795 (1994).

[23] P. Keblinski, A. Maritan, F. Toigo, and J. R. Banavar, Phys. Rev. Lett. **40**, 1783 (1995).

[24] M. Kardar, G. Parisi, and Y. Zhang, Phys. Rev. Lett. **56**, 889 (1986).

[25] L. Golubovic and R. P. U. Karunasiri, Phys. Rev. Lett. **66**, 3156 (1991).

[26] P. C. Hohenberg and B. I. Halperin, Rev. Mod. Phys. **49**, 435 (1977).

[27] T. M. Rogers, K. R. Elder, and R. C. Desai, Phys. Rev. B **37**, 9638 (1988).

[28] J. M. Kim and J. M. Kosterlitz, Phys. Rev. Lett. **62**, 2289 (1989); J. M. Kim, J. M. Kosterlitz, and T. Ala-Nissila, J. Phys. A **24**, 5569 (1991); K. Moser, J. Kertesz, and D. E. Wolf, Physica A **178**, 215 (1991), obtain $\beta=0.24\pm0.005$ in $d=2+1$ by a direct numerical integration of the KPZ equation.

[29] D. Y. K. Ko and F. Seno, Phys. Rev. E **50**, R1741 (1994).

[30] A. Mazor, D. J. Srolovitz, P. S. Hagan, and B. G. Bukiet, Phys. Rev. Lett. **60**, 424 (1988); D. J. Srolovitz, A. Mazor, and B. G. Bukiet, J. Vac. Sci. Technol. A **6**, 2371 (1988).

[31] D. J. Eaglesham, H. J. Gossman, and M. Cerullo, Phys. Rev. Lett. **65**, 1227 (1990).

[32] R. S. Williams, R. Bruinsma and J. Rudnik, in *Surface Disordering Growth, Roughening and Phase Transitions,* edited by R. Jullien, J. Kertesz, P. Meakin, and D. E. Wolf (Nova, New York, 1993).

[33] R. Messier and A. Roy, J. Vac. Sci. Technol. **13**, 1060 (1976); J. R. Blanco, R. Messier, K. Vedam and P. J. McMarr, in *Plasma Synthesis and Etching of Electronic Materials,* edited by R. P. H. Chang and P. Abeles, MRS Symposia Proceedings No. 38 (Materials Research Society, Pittsburgh, 1985), p. 301.

[34] C. Tang and S. Liang, Phys. Rev. Lett. **71**, 2769 (1993); S. Redner (unpublished) has carried out lattice simulations analogous to our two-rain case at grazing incidence, and has found patterns of independent growing trees that do not show any coalescence. These results suggest that there may be essential differences between the lattice and continuum models in this limit. We are grateful to Sid Redner for bringing his work to our attention.

[35] Y. Kuramoto, Suppl. Prog. Theor. Phys. **64**, 346 (1978); G. Sivashinsky, Acta Austronautica **4**, 1177 (1977).

[36] M. Marsili, A. Maritan, F. Toigo, and J. R. Banavar (unpublished).
[37] T. Ihle and H. Muller-Krumbhaar, Phys. Rev. Lett. **70**, 3083 (1993).
[38] The interaction term is similar to that studied in annihilation chemical reactions; see, e.g., K. Kang and S. Redner, Phys. Rev. A **32**, 435 (1985), and references therein.
[39] J. S. Langer, in *Directions in Condensed Matter Physics,* edited by G. Grinstein and G. Mazenko (World Scientific, Singapore, 1986), pp. 164–186; J. B. Collins and H. Levine, Phys. Rev. B **31**, 6119 (1985); G. Caginalp, Phys. Rev. A **39**, 887 (1989).
[40] For numerical work on the phase field model, see A. A. Wheeler, B. T. Murray, and R. J. Schaefer, Physica D **66**, 143 (1993); R. Kobayashi, *ibid.* **63**, 410 (1993).
[41] M. Nauenberg, R. Richter, and L. M. Sander, Phys. Rev. B **28**, R1649 (1983); G. Parisi and Y. C. Zhang, J. Stat. Phys. **41**, 1 (1985); D. Elderfield, J. Phys. A **18**, L773 (1985); Y. Shapir *ibid.* **18**, L970 (1985); H. Levine and Y. Tu, Phys. Rev. E **48**, R4207 (1993).
[42] L. M. Sander, in *Fractals In Physics* (Ref. 11), especially Fig. 2 on p. 245.
[43] W. W. Mullins and R. F. Sekerka, J. Appl. Phys. **35**, 444 (1964); J. S. Langer, Rev. Mod. Phys. **52**, 1 (1980).
[44] P. Z. Wong, Phys. Today **41**(12), 24 (1988); D. Bensimon, L. P. Kadanoff, S. Liang, B. I. Shraiman, and C. Tang, Rev. Mod. Phys. **58**, 997 (1986).
[45] E. Brener, H. Muller-Krumbhaar, and D. Temkin, Europhys. Lett. **17**, 535 (1992).
[46] O. Shochet, K. Kasser, E. Ben-Jacob, S. G. Lipson, and H. Muller-Krumbhaar, Physica A **181**, 136 (1992).
[47] R. Bausch, V. Dohm, H. K. Janssen, and R. K. P. Zia, Phys. Rev. Lett. **47**, 1837 (1981).
[48] A. Maritan, F. Toigo, J. Koplik, and J. R. Banavar, Phys. Rev. Lett. **69**, 3193 (1992).

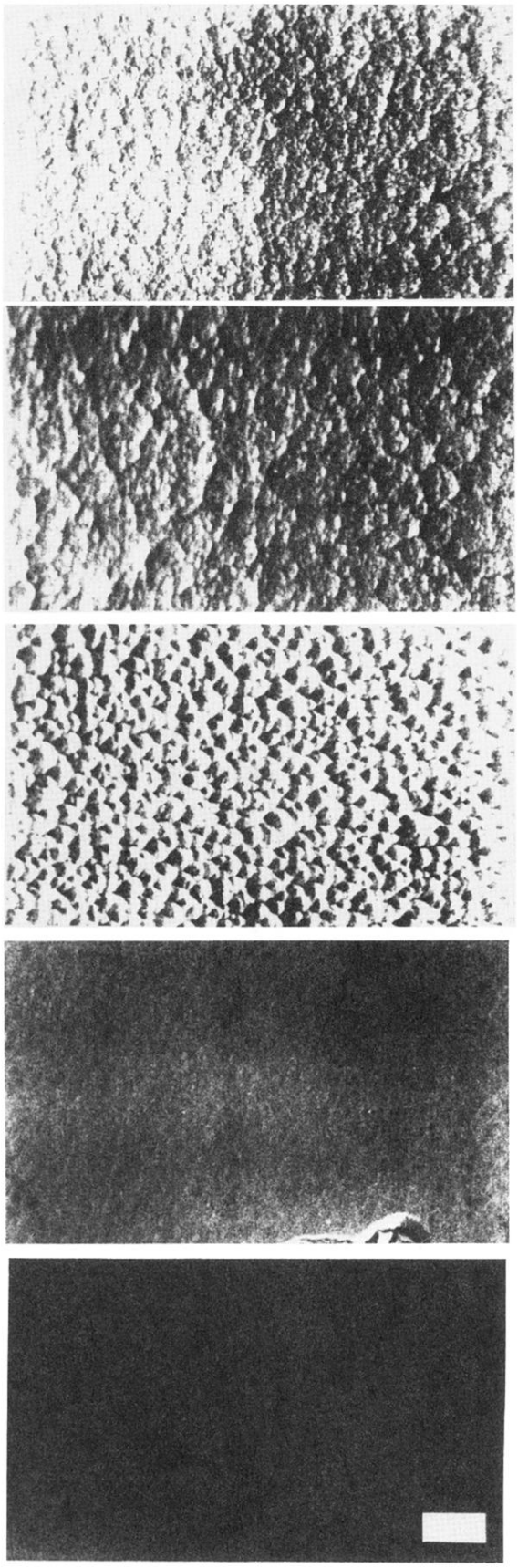

FIG. 10. Scanning electron micrographs of the top interfaces of sputter deposited amorphous germanium. The white bar marker denotes 1 μm.

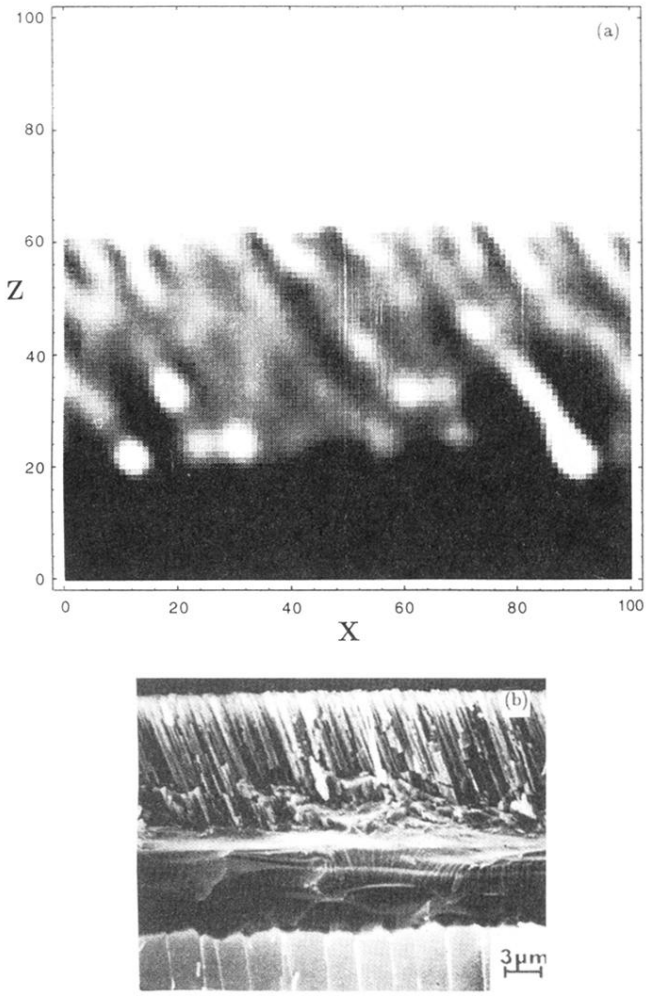

FIG. 12. (a) Density profiles for ballistic flux arriving at angle 45° with respect to the vertical direction on a one-dimensional substrate. Intensity of the flux $g_0|\mathbf{A}|=4$ and $a=1$. The white region corresponds to $f=-1$, while the darkest region denotes $f=+1$. (b) Scanning electron micrograph of the cross section of a 20 μm-thick a-Ge film showing the substrate (bottom) and both unetched (middle) and chemically etched morphology (top) revealing the internal, anisotropic density fluctuations. The columnar units are inclined at 20° with respect to the substrate normal.

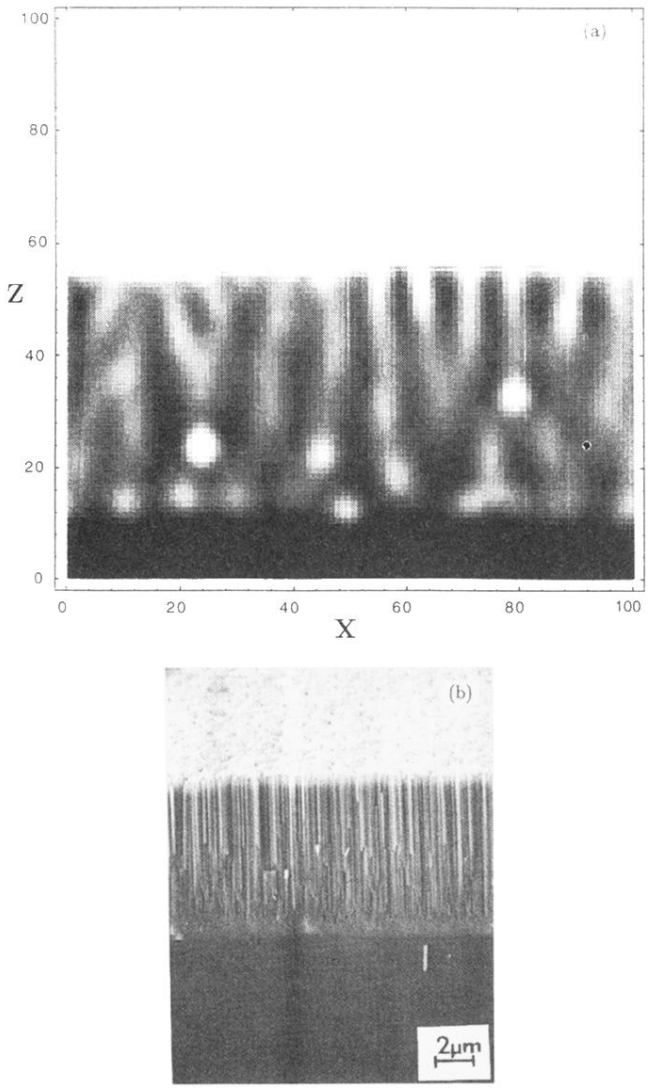

FIG. 14. (a) Same as Fig. 11(a), but with two ballistic fluxes arriving symmetrically toward the interface both at an angle of 70° with respect to the vertical direction ($g_0|\mathbf{A}_1|=g_0|\mathbf{A}_2|=5$). (b) Scanning electron micrograph of a 20-μm-thick film in which the anisotropic columnar morphology (middle) is normal to the substrate surface and parallel to the average incident angle of the depositing vapor species.

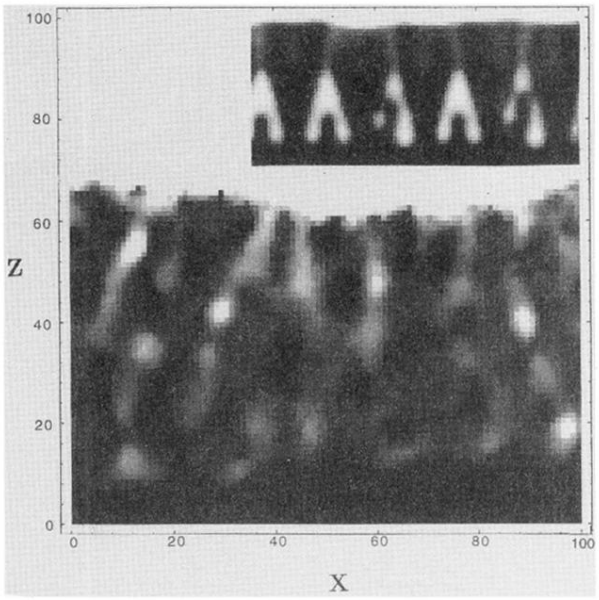

FIG. 7. Density profiles for vertical rain deposition growth (darkest regions correspond to $f=1$). The surface tension coefficient $a=\frac{1}{2}$; $A_z g_0=4.0$. The inset shows the growth of an initially structured substrate without the noise term present.